II. PLASMA DYNAMICS

II-A. PLASMA PHYSICS*

Prof. S. C. Brown
Prof. W. P. Allis
Prof. G. Bekefi
Prof. D. J. Rose
Prof. D. R. Whitehouse
Dr. S. Gruber
V. Arunasalam
C. D. Buntschuh
J. F. Clarke
J. D. Coccoli
E. W. Fitzgerald, Jr.
P. J. Freyheit
J. C. Ingraham
W. R. Kittredge
J. J. McCarthy
W. J. Mulligan
J. J. Nolan, Jr.
J. C. Terlouw
R. E. Whitney

1. ARC DISCHARGE IN CESIUM VAPOR

Attempts to make a highly ionized cesium plasma by using surface ionization have recently been reported.[1-3] Because of the low ionization potential of cesium, however, (3.87 volts for the first degree of ionization) it is also possible to produce a high percentage of ionization in the positive column of an arc discharge with a high current density at low pressures in cesium vapor.[4, 5]

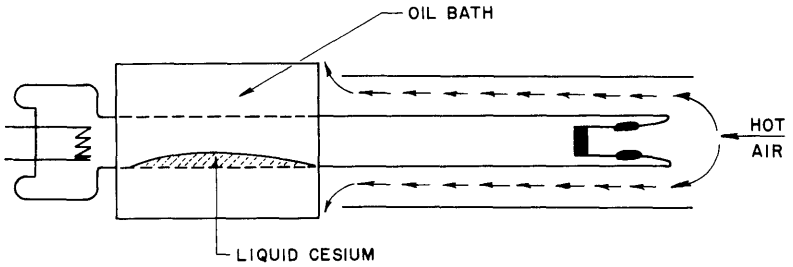

Fig. II-1. Cesium discharge tube.

In order to do this, we constructed a tube as shown schematically in Fig. II-1. We used an oxide-coated cathode with an emission capacity up to 5 amps and a molybdenum anode. The parts of the tube that are left and right of the oil bath are kept at a temperature higher than the oil temperature, by making use of heating tape and hot air, respectively.

The tube was baked out at 250°C when the cesium was still in a capsule. (At higher temperatures the cesium would attack the glass.) After breaking the capsule, the pressure in the tube was approximately 10^{-6} mm Hg, the cesium vapor pressure at room temperature.

---

*This work was supported in part by the Atomic Energy Commission under Contract AT(30-1)-1842; and in part by the Air Force Cambridge Research Center under Contract AF19(604)-5992; and in part by the National Science Foundation under Grant G-9330.

The pressure in the sealed-off tube is essentially determined by the temperature of the oil bath (Silicone oil DC 550), provided that the length of the oil bath is several mean-free paths of the cesium atoms. A dc magnetic field was applied along the axis of the tube.

An arc discharge in the tube produced an electron density of $2 \times 10^{13}/cm^3$ at pressures of 3×10^{-3} mm Hg, and higher. The density measurements were performed by propagating microwave energy through the discharge, and when the microwave propagation was just cut off it was assumed that $\omega = \omega_p$, where ω is the radian frequency of the microwave signal, and ω_p is the plasma frequency.

In order to cover a density range from 10^{12} to $1.8 \times 10^{13}/cm^3$, it was necessary to use X-band, K-band, and KA-band energy. A phase-shift technique for measuring the electron density could not be used because of the difficulty of matching the large tube to the small KA-band waveguide.

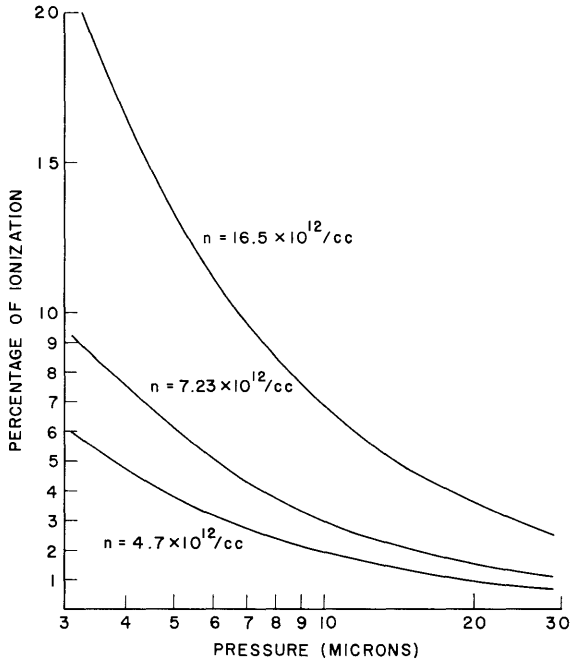

Fig. II-2. Percentage of ionization as a function of pressure at various electron densities.

The measured percentages of ionization in the positive column of the discharge as a function of the pressure are shown in Fig. II-2.

It is to be expected that at higher ionization percentages Coulomb interactions in the discharge play a dominant role.

Using the formula

$$\nu_{e-i} = 4\pi n v^{-3}\left[e^2/4\pi\epsilon_o m\right]^2 C_7$$

where

ν_{e-i} = electron-ion collision frequency,
n = electron density,
v = electron velocity,
e = electron charge,
m = electron mass, and
C_7 = Spitzer's diffusion length[6] for which we insert $\ell n\Lambda = 7$,

we obtain, at a density of 1.65×10^{33}/cc,

$$\nu_{e-i} = 1.27 \times 10^9/\text{sec}.$$

Here the electron temperature is estimated to be 0.5 ev.[4,5]

If electron-neutral collisions are dominant, we have

$J = nev_d = ne\frac{e}{m\nu_c}E$ and $\nu_c \propto E/J$, where J is the current density, E is the voltage per unit length, ν_c is the electron-neutral collision frequency, and the assumption is made that the electron temperature does not change with the pressure. It is to be expected that the electron temperature would decrease with pressure, but in the case under consideration this is thought to be a small effect.

At a pressure of 9 microns we measured $\nu_c = 1.35 \times 10^9$, at a density of 1.65×10^{13}/cc.

The collision frequencies for electron-neutral and electron-ion collisions seem to be approximately equal at this pressure, density, and temperature. Consequently, at lower pressures (but with the same density) we expect the discharge to be controlled by Coulomb interactions, hence with little dependence upon pressure, whereas at higher pressures electron-neutral collisions should be dominant and therefore E/J should be approximately proportional to the pressure p.

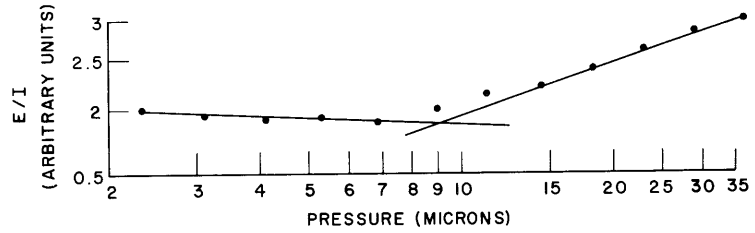

Fig. II-3. E/I as a function of pressure at an electron density of 1.65×10^{13}/cc. (Magnetic field, 700 gauss.)

Figure II-3 shows the results of a measurement which seem to be in agreement with this theoretical prediction.

In order to investigate the characteristics of the discharge more accurately, it is necessary to determine the electron temperature by direct measurement, and also to attempt to vary the electron temperature. The experiment will proceed in this way.

J. C. Terlouw

References

1. R. B. Hall and B. Brandt, Cesium vapor techniques in the production of fully ionized plasmas, Quarterly Progress Report No. 59, Research Laboratory of Electronics, M. I. T., October 15, 1960, pp. 9-14.

2. N. Rynn and N. D'Angelo, Rev. Sci. Instr. 31, 1326-1333 (1960).

3. R. C. Knechtili and J. Y. Wada, Phys. Rev. Letters 6, 215-217 (1961).

4. F. L. Mohler, J. Research Natl. Bur. Standards 19, 447-559 (1937).

5. R. K. Steinberg, A Probe Study of Arcs in Cesium Vapor, Ph.D. Thesis, Department of Physics, M. I. T., 1949.

6. L. Spitzer, Jr., Physics of Fully Ionized Gases (Interscience Publishers, Inc., New York, 1956), p. 73.

2. MAGNETOAMBIPOLAR DIFFUSION

Ambipolar diffusion currents in a magnetized plasma have been calculated[1] for a cylindrical metal cavity in which the radial wall is insulated from the end walls. The normal-mode solution for the plasma density is

$$n = n_o J_o(r/\Lambda_r) \cos(z/\Lambda_z)$$

where n_o is the density at the center of the cavity, and $\Lambda_r = R/2.405$, $\Lambda_z = L/\pi$, with R and L the radius and length of the cavity. The ion and electron currents are given by

$$\bar{\Gamma}_\pm = \bar{i}_r \Gamma_{\pm R} J_1(r/\Lambda_r) \cos(z/\Lambda_z) + \bar{i}_z \Gamma_{\pm Z} J_o(r/\Lambda_r) \sin(z/\Lambda_z)$$

with the coefficients $\Gamma_{\pm R}$ and $\Gamma_{\pm Z}$ given by

$$\frac{\Gamma_{\pm R}}{n_o D_a \Lambda_r} = \frac{b_a}{\Lambda_r^2} \pm \left(\frac{\nu_i}{D_a} - \frac{b_a}{\Lambda_r^2} - \frac{1}{\Lambda_z^2} \right) \frac{\mu_\mp}{(\mu_- - \mu_+)(1-b_\mp)}$$

$$\frac{\Gamma_{\pm Z}}{n_o D_a \Lambda_z} = \frac{1}{\Lambda_z^2} \mp \left(\frac{\nu_i}{D_a} - \frac{b_a}{\Lambda_r^2} - \frac{1}{\Lambda_z^2} \right) \frac{\mu_\pm}{(\mu_- - \mu_+)(1-b_a)}$$

where ν_i is the electron ionization frequency, $\mu_\pm$ are the ion and electron mobilities, D_a is the ambipolar diffusion coefficient, and b is the quenching factor which for ion,

electron, and ambipolar quenching is given by

$$b_{\pm} = \frac{1}{1 + \mu_{\pm}^2 B^2}, \quad b_a = \frac{1}{1 + \mu_+ \mu_- B^2}.$$

If an external electrical connection is made from the radial to the end walls, an unbalance of electron and ion currents can flow to either wall and constitute an electrical current through the external circuit. The particle current difference obtained from the equations above is

$$\frac{\Gamma_{-Z} - \Gamma_{+Z}}{n_o D_a \Lambda_z} = \frac{\Gamma_{+R} - \Gamma_{-R}}{n_o D_a \Lambda_r} = \left(\frac{\nu_i}{D_a} - \frac{b_a}{\Lambda_r^2} - \frac{1}{\Lambda_z^2} \right) \frac{(\mu_- + \mu_+)}{(\mu_- - \mu_+)(1 - b_a)}$$

and thus varies directly with the ionization frequency, ν_i. The current cannot be changed indefinitely, however, as a limit will be reached when $\Gamma_{\pm Z}$ or $\Gamma_{\pm R}$ goes to zero. A table of these limits with the corresponding values of ν_i/D_a is given in Table II-I. The open-circuit (congruence) and short-circuit conditions are also indicated.

Table II-I. Ionization frequency limits.

Condition	Values of ν_i/D_a
$\Gamma_{+Z} = 0$ Limit (Allis)	$\frac{b_a}{\Lambda_r^2} + \frac{b_a}{b_- \Lambda_z^2}$
$\Gamma_{-R} = 0$ Limit (Simon)	$\frac{b_+}{\Lambda_r^2} + \frac{1}{\Lambda_z^2}$
Short-circuit	not determined
Open-circuit $\Gamma_+ = \Gamma_-$ (congruence)	$\frac{b_a}{\Lambda_r^2} + \frac{1}{\Lambda_z^2}$
$\Gamma_{+R} = 0$ Limit	$\frac{b_-}{\Lambda_r^2} + \frac{1}{\Lambda_z^2}$
$\Gamma_{-Z} = 0$ Limit	$\frac{b_a}{\Lambda_r^2} + \frac{b_a}{b_+ \Lambda_z^2}$

For a steady-state discharge, therefore, the ionization frequency, and hence the required power is determined by the current in the external circuit. The potential

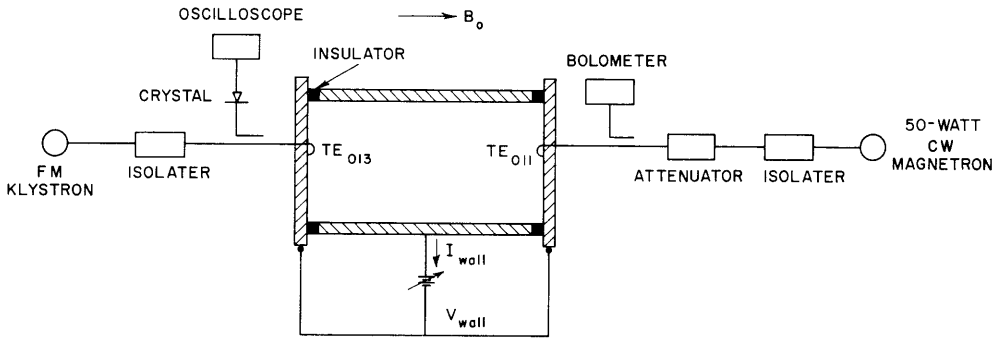

Fig. II-4. Vacuum cylindrical cavity.

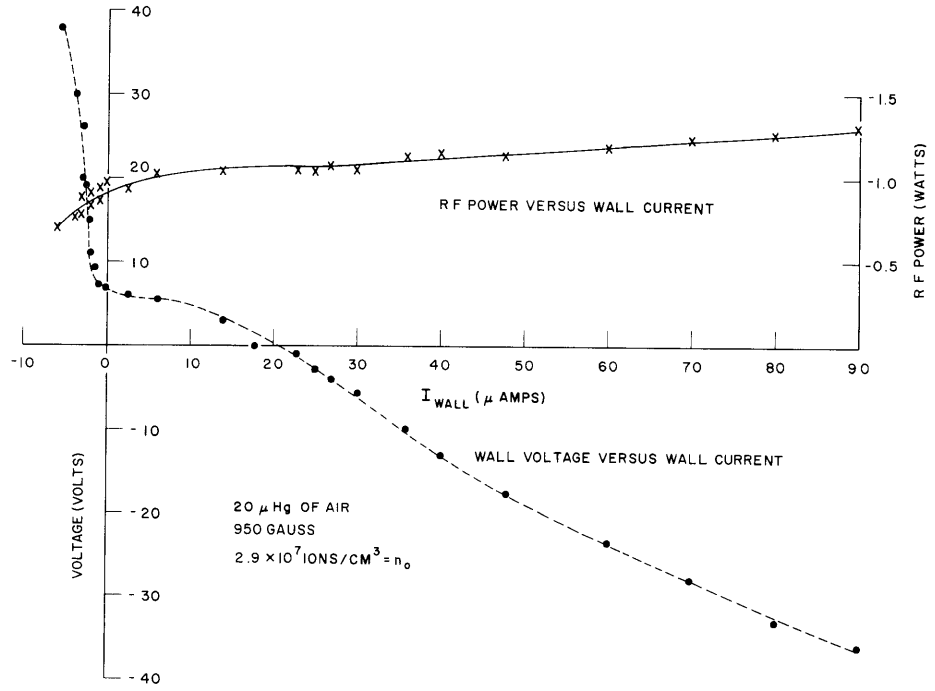

Fig. II-5. Experimental data.

difference between the walls also changes with the current and is determined by the required space-charge field in the plasma and the sheath. The fields in the plasma are easily calculated, but work is still in progress to determine the potential drop in the sheaths.

An experimental vacuum metal cavity was designed and built to test the preceding theory. The cavity was 12.7 cm in diameter and 64.3 cm in length, and also served as a microwave cavity operating in the TE_{011} mode at 3000 mc, as shown in Fig. II-4. The TE_{013} mode was used to measure the electron density. Preliminary data are shown in

Fig. II-5 in which the voltage from radial to end walls is plotted against the current. Throughout the run, the density was kept constant by adjusting the microwave power into the cavity; this power is also shown plotted as a function of the current in Fig. II-5. The experimental data are in good qualitative agreement with the theory. The small negative saturation current is predicted for large positive voltages, together with a minimum in the ionization frequency or microwave power at the $\Gamma_{+R} = 0$ limit. As the current increases, the required power increases, and the voltage decreases through the congruence and short-circuit conditions until eventually the current tends to saturate at the $\Gamma_{-R} = 0$ limit. The ratio of positive-to-negative saturation currents is given approximately by μ_-/μ_+. Further analysis of these data is in progress.

Energy conversion from microwave to direct current is seen to take place when the voltage and current are both positive. Calculations are also being made to see for what parameters this conversion efficiency is maximum.

D. R. Whitehouse, H. B. Wollman

References

1. D. R. Whitehouse, Magnetoambipolar diffusion, Quarterly Progress Report No. 57, Research Laboratory of Electronics, M. I. T., April 15, 1960, pp. 20-23.

II-B. PLASMA ELECTRONICS*

Prof. L. D. Smullin	W. D. Getty	C. L. Salter, Jr.
Prof. H. A. Haus	W. G. Homeyer	A. J. Schneider
Prof. A. Bers	H. Y. Hsieh	P. E. Serafim
Prof. D. J. Rose	A. J. Impink, Jr.	P. S. Spangler
Prof. T. H. Dupree	P. W. Jameson	A. W. Starr
P. Chorney	W. Larrabee IV	J. S. Tulenko
J. R. Cogdell	L. M. Lidsky	M. C. Vanwormhoudt
L. J. Donadieu	D. L. Morse	R. C. Wingerson
T. J. Fessenden	R. J. Pellar	S. Yoshikawa
	S. D. Rothleder	

1. THERMAL NOISE FROM PLASMAS

This study has been completed by M. C. Vanwormhoudt. In August 1961, he submitted the results to the Department of Electrical Engineering, M. I. T., as a thesis in partial fulfillment of the requirements for the Degree of Doctor of Science.

H. A. Haus

2. POWER FLOW ALONG A CIRCUIT

Consider a one-dimensional plasma coupled to resistively loaded coils as described by Haus.[1] It is clear that in the absence of the plasma the coils are completely uncoupled and cannot propagate power. The presence of the plasma, however, couples the coils so as to produce a "circuit-beam transmission line" capable of propagating power. This interpretation stems from the appearance in the small-signal power theorem of a term that represents propagated power.

The small-signal complex power theorem (cf. Haus[2]) for a one-dimensional plasma moving through a transverse magnetic field is

$$\frac{d}{dz}\left(-\frac{EB^*}{2\mu_o} + P_p\right) + 2j\omega\left(\frac{|B|^2}{4\mu_o} + U_p\right) + \frac{EJ_d^*}{2} = 0 \tag{1}$$

where

$$P_p = \frac{1}{2}(\rho_o v + v_o \rho)\left(v_o v + \frac{p}{\rho_o}\right)^* \tag{2}$$

and

$$U_p = \frac{1}{4}\frac{\gamma p_o}{\rho_o^2}|\rho|^2 - \frac{1}{4}\rho_o|v|^2. \tag{3}$$

Here P_p is the small-signal complex power density carried by the plasma, U_p is the

---

*This work was supported in part by the National Science Foundation under Grant G-9330.

difference between a compressional and a kinetic pseudo-energy density, and $EJ_d^*/2$ is the complex power per unit volume given up by the plasma to the source of the driving-current density J_d. Let $P = -EB^*/2\mu_o + P_p$, and $U = |B|^2/4\mu_o + U_p$. Then Eq. 1 becomes

$$\frac{dP}{dz} + 2j\omega U + \frac{EJ_d^*}{2} = 0. \tag{4}$$

For the resistively loaded coils of Haus,[1] we have

$$J_d = -\frac{dI}{dz}, \quad E = wV, \quad \text{and} \quad \frac{dV}{dz} = \frac{I}{g}. \tag{5}$$

By using Eqs. 5, the power per unit volume given up by the plasma can be written

$$\frac{EJ_d^*}{2} = \frac{w|I|^2}{2g} - w\frac{d}{dz}\left(\frac{VI^*}{2}\right) \tag{6}$$

Equation 6 tells us that of the power per unit volume, $1/2\ EJ_d^*$, given up by the plasma, only part of it, $w|I|^2/2g$, is dissipated in the resistance; the remainder, the term containing VI^*, represents propagated power.

According to the power theorem, $-wd/dz\,(VI^*/2)$ is power given up by the plasma. We are considering one-dimensional power flow only, so that both this power and the power carried by the plasma itself must be thought of as propagating in the same space.

In the limit of weak coupling, the waves propagate as $e^{-j(\beta+\delta)z}$, where $j\beta$ is the propagation constant in the unperturbed plasma, and δ is a small (imaginary) number. If in Eq. 5 we replace d/dz by $-j(\beta+\delta)$, we have to first order in δ,

$$\frac{EJ_d^*}{2} = \frac{w|I|^2}{2g}\left(1 - \frac{2\delta}{\beta}\right). \tag{7}$$

In the limit $\delta \to 0$, all of the power supplied by the plasma is dissipated. No power is propagated by the "circuit-beam" system.

Other one-dimensional circuits coupled to plasma beams exhibit similar "circuit-beam" power terms. The simple transmission line coupled to a plasma[3] is an example.

A. J. Schneider

References

1. H. A. Haus, Magnetohydrodynamic ac generators, Quarterly Progress Report No. 62, Research Laboratory of Electronics, M. I. T., July 15, 1961, pp. 31-33.

2. H. A. Haus, Magnetohydrodynamic ac generators, Quarterly Progress Report No. 60, Research Laboratory of Electronics, M. I. T., January 15, 1961, p. 48.

3. H. A. Haus, Quarterly Progress Report No. 60, op. cit., see Fig. II-18, p. 49.

3. INTERACTION OF AN ELECTRON BEAM WITH PLASMA*

In our previous report[1] we studied the interaction of ions and electrons in a plasma. In this report we shall examine the interaction of an electron beam with a plasma. Our model for the plasma is one with ions of negligible thermal velocities and electrons with a thermal spread of velocities, with and without a superimposed drift velocity. The velocity distribution is very nearly Maxwellian. We have used this type of velocity distribution, as well as two other types: a resonant type of curve and a square distribution. The latter has proved to be very useful in our computations.

We have worked on the one-dimensional case and on the case with finite geometry. In both cases, after an exact formulation based on small-signal theory, we have used reasonable approximations, in order to find solutions to the dispersion equations.

We have neglected the effects of pressure gradients and collisions throughout this first treatment. We have also assumed uniform spatial density for ions and electrons.

a. One-Dimensional Model

i. Dispersion Equation

We derive the dispersion equation, using the well-known formulation of the small-signal theory as it has been modified for a continuous distribution of velocities by Vlasov, Landau, and Allis.

$$\sum_i \omega_{pi}^2 \int_{-\infty}^{\infty} \frac{f_i(v)\,dv}{(\omega - v\beta)^2} = 1 \tag{1}$$

where ω_{pi} is the plasma frequency of the i^{th} component of the plasma corresponding to its total density n_i, $f_i(v)$ is the normalized velocity distribution, ω is the angular frequency, and β is the wave number.

Maxwellian Distribution

$$f_e(v) = \left(\frac{m_e}{2\pi k T_e}\right)^{1/2} \exp\left[-\frac{m_e(v-v_{me})^2}{2kT_e}\right] = \frac{1}{\sqrt{2\pi}\,v_{pe}} \exp\left[-\frac{(v-v_{me})^2}{2v_{pe}^2}\right] \tag{2}$$

where k is Boltzmann's constant, v_{me} is the mean velocity and $v_{pe}^2 = kT_e/m_e$. The dispersion law 1 can be written

---

*This research was supported in part by Purchase Order DDL B-00306 with Lincoln Laboratory, a center for research operated by Massachusetts Institute of Technology, with the joint support of the U.S. Army, Navy, and Air Force under Air Force Contract AF19(604)-7400.

$$\frac{\omega_{pi}^2}{\omega^2} + \frac{\omega_{pb}^2}{(\omega - v_b\beta)^2} + \omega_{pe}^2 \int_{-\infty}^{\infty} \frac{f_e(v)\,dv}{(\omega - v\beta)^2} = 1$$

where i stands for ions, e for electrons in the plasma, and b for electrons in the beam.

By contour integration, we obtain for $\beta v_{me}/\omega \ll 1$ and $v_{me} \ll v_{pe}$:

$$\frac{\omega_{pi}^2}{\omega^2} + \frac{\omega_{pb}^2}{(\omega - v_b\beta)^2} + \frac{\omega_{pe}^2}{(\omega - v_{me}\beta)^2}\left[1 + 3\frac{\beta^2 v_{pe}^2}{\omega^2}\right] = 1 \tag{3a}$$

or

$$\frac{\omega_{pb}^2}{(\omega - v_b\beta)^2} + \frac{\omega_{pe}^2}{\omega^2}\left(2\frac{\beta v_{me}}{\omega} + 3\frac{\beta^2 v_{pe}^2}{\omega^2}\right) = \frac{\omega^2 - \omega_{pi}^2 - \omega_{pe}^2}{\omega^2} \tag{3b}$$

or

$$\frac{\omega_{pb}^2}{(\omega - v_b\beta)^2} + \frac{\omega_{pe}^2}{\omega^2 - 2\beta v_{me}\omega - 3\beta^2 v_{pe}^2} = \frac{\omega^2 - \omega_{pi}^2}{\omega^2}\,. \tag{3c}$$

when ω/β is very nearly real (very small decay) we have to add for the integral for electrons the imaginary term

$$\frac{j\pi\omega_{pe}^2}{\beta^2}\frac{df_e}{dv}\left(\frac{\omega}{\beta} - v_{me}\right)$$

which is the familiar Landau damping term.[2]

Square Distribution

If ω/β is different from $(-v_o + v_{me})$ and $(v_o + v_{me})$, the dispersion equation is

$$\frac{\omega_{pb}^2}{(\omega - v_b\beta)^2} + \frac{\omega_{pe}^2}{(\omega - \beta v_{me})^2 - \beta^2 v_o^2} = \frac{\omega^2 - \omega_{pi}^2}{\omega^2} \tag{4}$$

where v_o is the halfwidth of the square distribution. Under the usual assumption $\left(v_{me} \ll v_o,\ \text{and}\ \beta^2\overline{v^2}/\omega^2 \ll 1\right)$, Eq. 4 is just the same as Eq. 3c if $v_o = \sqrt{3}\,v_{pe}$.

(ii) Solutions of the Dispersion Equation

We define the quantities

$$N = \frac{\omega_{pb}}{\omega_{pe}} = \left(\frac{n_b}{n_e}\right)^{1/2} \tag{5a}$$

$$\ell = \frac{v_b}{v_o}, \quad \ell_m = \frac{v_{me}}{v_o}. \tag{5b}$$

At $\omega = \omega_{pi}$ we have the pairs of solutions to Eq. 4:

$$\beta = \frac{\omega_{pi}}{v_o}\left[\frac{\ell^2 + N^2\ell_m \pm jN\left[\ell^2 - N^2 - 1 - \ell_m(2\ell - \ell_m)\right]^{1/2}}{\ell^2 - N^2(1-\ell_m)}\right] \tag{6a}$$

and

$$\beta = \pm\infty \tag{6b}$$

For $\ell_m \ll 1$, and $\ell \gg 1 + N^2$, we find

$$\beta \cong \frac{\omega_{pi}}{v_b}(1 \pm jN) \tag{6c}$$

For ω different from ω_{pi} but in the neighborhood, we get

$$\beta \cong \beta_{eb}\left\{1 \pm j\frac{\omega_{pb}}{\left(\omega_{pe}^2 + \omega_{pi}^2 - \omega^2\right)^{1/2}}\right\} \tag{7a}$$

and

$$\beta \cong \pm\left[\frac{\beta_{pe}^2 - \beta_{pb}^2 + \Delta^2\beta_{ee}^2 + \left[\left(\beta_{pe}^2 + \beta_{pb}^2 + \Delta^2\beta_{ee}^2\right)^2 - 4\beta_{pe}^2\beta_{pb}^2\right]^{1/2}}{2\Delta^2}\right]^{1/2} \tag{7b}$$

where

$$\Delta^2 = \frac{\omega_{pi}^2 - \omega^2}{\omega^2}.$$

Bohm and Gross[3] find results that are different from ours. They assert that if $\beta \gg \beta_{eb}$, it cannot be complex. This proof neglects the ion plasma frequency and makes use of the nonvalid expansion of $1\Big/\left(\omega^2 - \beta^2 v_o^2\right)$ into a power series of $(\beta v_o/\omega)^2$. As is evident, the resulting series diverges for large β. Equation 7b shows the existence of a passband for $\omega < \omega_{pi}$, even in the one-dimensional case.

b. Two-Dimensional Model

We shall consider a hollow uniform cylindrical metal tube, whose axis is taken as the z-direction. We consider also the effect of a uniform, finite, axial magnetostatic field B_o. We assume that the plasma has a uniform density of ions. Electrons have thermal velocities and are neutralized by finite mass ions.

(i) General Dispersion Equation

We use a matrix formulation, but we shall consider as variable the electric field instead of the velocities,[4] since now we have an infinite number of velocities. It will be useful to define all vectors as column matrices and we shall use the superscript T for the transpose of a matrix. Finally, we define the operator F_v with the meaning $F_v \cdot a(v) = \int_{-\infty}^{\infty} f(v)\, a(v)\, dv$.

Space and time dependences of the waves are given by $\exp j(\omega t - \bar{\beta}\bar{r})$. From Maxwell's equations we get

$$\nabla^2 \bar{E} + k^2 \bar{E} = j\omega\mu_o \bar{J} + \frac{\nabla\rho}{\epsilon_o} \tag{8}$$

where $k^2 = \omega^2/c^2$. For the charge density we obtain

$$\rho = j[\beta]^T \left\{ \frac{\rho_{ob}\eta_b}{\omega - \beta_z v_{ob}} [M_b] + \frac{\rho_{oi}\eta_i}{\omega} [M_i] + \rho_{oe}\eta_e F_{v_{oe}} \cdot \left(\frac{[M_e]}{\omega - \beta_z v_{oe}} \right) \right\} [E] \tag{9a}$$

For the current density we find

$$[J] = j \left\{ \rho_{oi}\eta_i [M_i] + \rho_{ob}\eta_b \left(1 + \frac{v_{ob}}{\omega - \beta_z v_{ob}} [i_z][\beta]^T \right) [M_b] \right.$$
$$\left. + \rho_{oe}\eta_e F_{v_{oe}} \cdot \left(\left(1 + \frac{v_{oe}}{\omega - \beta_z v_{oe}} [i_z][\beta]^T \right) [M_e] \right) \right\} [E] \tag{9b}$$

where $[M_i]$ (similarly for $[M_e]$ and $[M_b]$) is given by

$$[M_i] = \begin{bmatrix} \frac{\omega - \beta_z v_{oi}}{\omega_{ci}^2 - (\omega - \beta_z v_{oi})^2} & \frac{j\omega_{ci}}{\omega_{ci}^2 - (\omega - \beta_z v_{oi})^2} & 0 \\ \frac{-j\omega_{ci}}{\omega_{ci}^2 - (\omega - \beta_z v_{oi})^2} & \frac{\omega - \beta_z v_{oi}}{\omega_{ci}^2 - (\omega - \beta_z v_{oi})^2} & 0 \\ 0 & 0 & -\frac{1}{\omega - \beta_z v_{oi}} \end{bmatrix} \tag{10}$$

and $\omega_{ci} = -\eta_i B_o$.

If we substitute (9a) and (9b) in (8), we get the dispersion relation

$$\text{Determinant of} \left[(-\beta^2+k^2)[I] + \frac{\omega}{c^2} \left\{ \omega_{pi}^2[M_i] + \omega_{pb}^2 \left(1 + \frac{v_{ob}}{\omega - \beta_z v_{ob}} [i_z][\beta]^T \right) [M_b] + \omega_{pe}^2 F_{v_{oe}} \cdot \left(\left(1 + \frac{v_{oe}}{\omega - \beta_z v_{oe}} [i_z][\beta]^T \right) [M_e] \right) \right\} - [\beta][\beta]^T \left\{ \frac{\omega_{pb}^2}{\omega - \beta_z v_{ob}} [M_b] + \frac{\omega_{pi}^2}{\omega} [M_i] + \omega_{pe}^2 F_{v_{oe}} \cdot \left(\frac{[M_e]}{\omega - \beta_z v_{oe}} \right) \right\} \right] = 0 \tag{11}$$

The complete derivation of this dispersion equation and the values of the elements of matrix (10) are given in our internal memorandum.[5]

If we assume that the solution has a cylindrical symmetry (i.e., $\beta_\theta = 0$), that there are no thermal velocities, and that our case is quasistatic and nonrelativistic (i.e., $v^2/c^2 \ll 1$), we obtain Chorney's equation.[6]

$$\frac{\beta_z^2}{\beta_r^2} = \frac{1 + \dfrac{\omega_{pi}^2}{\omega_{ci}^2 - \omega^2} + \dfrac{\omega_{pe}^2}{\omega_{ce}^2 - \omega^2} + \dfrac{\omega_{pb}^2}{\omega_{ce}^2 - (\omega - v_o\beta_z)^2}}{-1 + \dfrac{\omega_{pi}^2}{\omega^2} + \dfrac{\omega_{pe}^2}{\omega^2} + \dfrac{\omega_{pb}^2}{(\omega - v_o\beta_z)^2}} \tag{12}$$

This equation has been solved for the absence of the beam.[7] We try now to solve it for the presence of the beam.

(ii) Solutions of the Dispersion Equation

We consider a completely filled waveguide. In this case, $\beta_r = a/r_o$, where a are the zeros of $J_o(a) = 0$, and r_o is the radius of the waveguide. We define the quantities

$$\beta_i^2 = \beta_r^2 \frac{1 + \dfrac{\omega_{pi}^2}{\omega_{ci}^2 - \omega^2} + \dfrac{\omega_{pe}^2}{\omega_{ce}^2 - \omega^2}}{-1 + \dfrac{\omega_{pi}^2 + \omega_{pe}^2}{\omega^2}} \tag{13a}$$

$$\beta_{ib}^2 = \beta_{pb}^2 \frac{\omega^2}{\omega_{pi}^2 + \omega_{pe}^2 - \omega^2}. \tag{13b}$$

Equation 12 can be written as

$$\left(\beta_z^2-\beta_i^2\right)\left[(\beta_z-\beta_e)^2-\beta_{ce}^2\right](\beta_z-\beta_e)^2+\beta_{ib}^2\left\{\beta_r^2(\beta_z-\beta_e)^2+\beta_z^2\left[(\beta_z-\beta_e)^2-\beta_{ce}^2\right]\right\}=0. \tag{14}$$

If we look for roots of the form $|\beta_z| \gg \beta_e$, we get

$$\beta_z^2=\frac{\left[\beta_{ce}^2+\left(\beta_i^2-\beta_{ib}^2\right)\right]\pm\left\{\left[\beta_{ce}^2-\left(\beta_i^2-\beta_{ib}^2\right)\right]^2-4\beta_{ib}^2\beta_r^2\right\}^{1/2}}{2}. \tag{15}$$

We see that

$$\beta_{ib}^2=\beta_e^2\,\frac{n_b/n_e}{1-\dfrac{\omega^2}{\omega_{pe}^2}}$$

If ω is in the vicinity of ω_{pe}, $|\beta_{ib}| \gg \beta_e$. Then we find

$$\beta_z=\frac{\omega}{v_o}\,\frac{1}{1\pm\dfrac{\beta_{pb}}{\beta_r A}} \tag{16}$$

where

$$A=\left[1+\frac{\omega_{pb}^2}{\omega_{ce}^2}+\frac{\omega_{pi}^2}{\omega_{ci}^2-\omega^2}+\frac{\omega_{pe}^2}{\omega_{ce}^2-\omega^2}\right]^{1/2}. \tag{16a}$$

Equations 15 and 16 are the complete solution for ω in the vicinity of $\omega_{pe}(\omega \gg \omega_{pi})$. For ω near ω_{pi} Eq. 15 is still valid, but gives roots near β_{ce}. However, in order to find the solutions for space-charge waves, we assume that $\beta_z = \beta_e + \delta$, with $\delta \ll \beta_e \ll \beta_{ce}$. Then Eq. 14 can be written

$$\delta^3+\left(\frac{\beta_e}{2}-\frac{\beta_i^2\beta_{ce}^2+\beta_r^2\beta_{ib}^2}{2\beta_e\beta_{ce}^2}\right)\delta^2+\beta_{ib}^2\delta+\frac{\beta_{ib}^2\beta_e}{2}=0. \tag{17}$$

At the intersection of the characteristic line for the slow space-charge wave of the beam $\beta_e + \beta_q$ and the characteristic line for the plasma[6] we have $\beta_i^2 = (\beta_e+\beta_q)^2$. Using the method of weak coupling, we may assume that one solution of Eq. 17 is $\delta = -\beta_q$. Then the other two solutions are given by

$$\delta^2-\left(2\beta_q+\frac{\beta_q^2}{2\beta_e}+\frac{\beta_r^2\beta_{ib}^2}{2\beta_e\beta_{ce}^2}\right)\delta+\frac{\beta_{ib}^2\beta_e}{2\beta_q}=0 \tag{18}$$

and

$$\delta = \left(\beta_q + \frac{\beta_q^2}{4\beta_e} + \frac{\beta_r^2\beta_{ib}^2}{4\beta_e\beta_{ce}^2}\right) \pm \left\{\left(\beta_q + \frac{\beta_q^2}{4\beta_e} + \frac{\beta_r^2\beta_{ib}^2}{4\beta_e\beta_{ce}^2}\right)^2 - \frac{\beta_{ib}^2\beta_e}{2\beta_q}\right\}^{1/2} \tag{19}$$

However, we know that $\beta_q \approx \beta_e\left(\frac{n_b}{n_e}\right)^{1/2}\frac{\beta_{pe}}{\beta_r}$, and $\beta_{ib} = \beta_e \cdot (n_b/n_e)^{1/2} \cdot \frac{\omega_{pe}}{\left(\omega_{pe}^2+\omega_{pi}^2-\omega^2\right)^{1/2}}$.

Therefore for $\beta_r \gg \beta_{pe}$, $\beta_{ce} > \beta_{pe}$,

$$\delta = \beta_q + \beta_e\frac{n_b}{4n_e}\frac{\beta_r^2}{\beta_{ce}^2}\frac{\omega_{pe}^2}{\omega_{pe}^2+\omega_{pi}^2-\omega^2} \pm j\beta_e\left\{\frac{1}{2}\left(\frac{n_b}{n_e}\right)^{1/2}\frac{\beta_r}{\beta_{pe}}\frac{\omega_{pe}^2}{\omega_{pe}^2+\omega_{pi}^2-\omega^2}\right.$$

$$\left. - \frac{1}{16}\left(\frac{n_b}{n_e}\right)^2\left(\frac{\beta_r}{\beta_{ce}}\right)^4\left(\frac{\omega_{pe}^2}{\omega_{pe}^2+\omega_{pi}^2-\omega^2}\right)^2\right\}^{1/2} \tag{20}$$

These roots predict amplification at frequencies a little larger than

$$\omega = \left(\omega_{ci}^2 + \frac{\omega_{pi}^2}{1+\frac{\omega_{pe}^2}{\omega_{ce}^2}}\right)^{1/2} . \tag{21}$$

P. E. Serafim

References

1. P. E. Serafim, Interaction of ions and electrons, Quarterly Progress Report No. 62, Research Laboratory of Electronics, M.I.T., July 15, 1961, pp. 46-52.

2. L. Landau, Jour. Appl. Phys. (USSR) 10, 25, 1946.

3. D. Bohm and E. P. Gross, Excitation and damping of plasma oscillation, Phys. Rev. 75, 1864 (1949).

4. L. D. Smullin and P. Chorney, Propagation in Ion Loaded Waveguides, Symposium on Electronic Waveguides, Polytechnic Institute of Brooklyn, New York, 1958, pp. 229-234.

5. P. E. Serafim, Interaction of Electron Beam and Plasma, Tube Laboratory Internal Memorandum, Research Laboratory of Electronics, M.I.T., September 1961.

6. P. Chorney, Quasi-Static Propagation in Multiparticle Waveguides, Tube Laboratory Internal Memorandum, Research Laboratory of Electronics, M.I.T., December 1959.

4. BACKWARD-WAVE OSCILLATIONS IN A BEAM-PLASMA SYSTEM*

Some calculations have been made[1] to determine whether backward-wave oscillations exist in a beam-plasma system as a result of the coupling between the negative-dispersion plasma waveguide wave and either the slow beam cyclotron wave or the slow beam space-charge wave. The physical system considered is a drift tube of radius a, which contains an electron beam of velocity v_o and a stationary plasma of electrons neutralized by heavy positive ions. A dc magnetic field B_o is applied parallel to the axis of the tube, as shown in Fig. II-6, and thermal velocities are ignored.

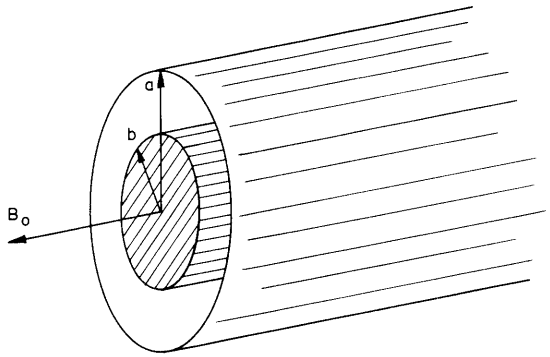

Fig. II-6. Beam and plasma-loaded waveguide.

In the cases considered, the electron cyclotron frequency ω_{ce} is greater than the plasma electron plasma frequency ω_{pp}, so the backward plasma waveguide wave occurs for $\omega > \omega_{ce}$. The dispersion relation, under the quasi-static assumption $\left(\beta_z^2 \gg \omega^2/c^2\right)$ has been shown by Smullin and Chorney[2] to be

$$\beta_z^2\left[1 - \frac{\omega_{pp}^2}{\omega^2} - \frac{\beta_{pb}^2}{(\beta_e - \beta_z)^2}\right] = \beta_T^2\left[\frac{\omega_{pp}^2 + \omega_{ce}^2 - \omega^2}{\omega^2 - \omega_{ce}^2} + \frac{\beta_{pb}^2}{(\beta_e - \beta_z)^2 - \beta_{ce}^2}\right] \tag{1}$$

where β_z is the longitudinal wave number, $\beta_e = \omega/v_o$, $\beta_{ce} = \omega_{ce}/v_o$, and $\beta_{pb} = \omega_{pb}/v_o$ is the beam plasma wave number. The longitudinal wave number β_T is given by $J_o(\beta_T a) = 0$ for the filled tube. When the partially filled tube is considered, Eq. 1 must be solved with a boundary-condition equation for a value of β_T with β_z.

*This research was supported in part by Purchase Order DDL B-00306 with Lincoln Laboratory, a center for research operated by Massachusetts Institute of Technology, with the joint support of the U.S. Army, Navy, and Air Force under Air Force Contract AF19(604)-7400.

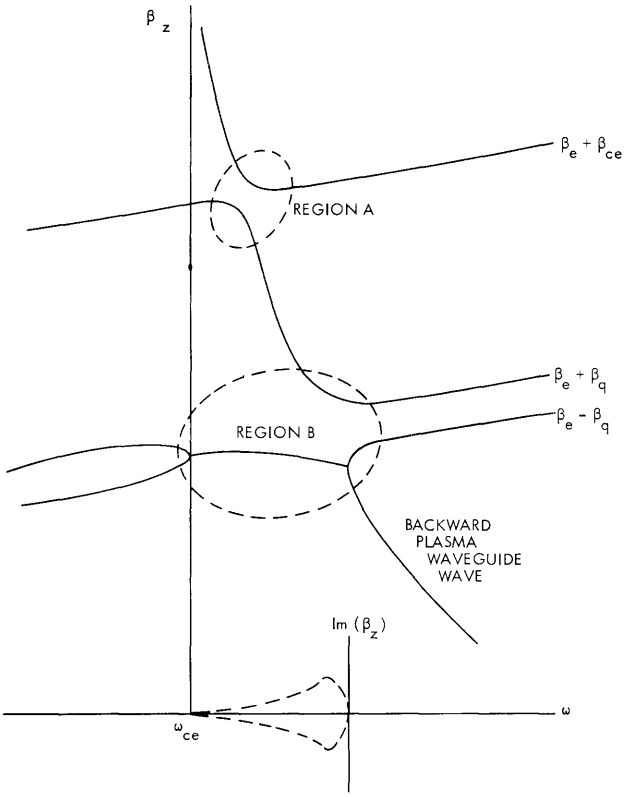

Fig. II-7. Computed beam-plasma dispersion curves ($\omega_{cc} > \omega_{pp}$).

Equation 1 has been solved numerically for the filled tube, and the results pertinent to the interactions discussed here are shown in Fig. II-7. Region A of Fig. II-7 shows the region of coupling between the backward plasma waveguide wave and the slow-beam cyclotron wave, and Region B shows the coupling between the backward plasma waveguide wave and the beam space-charge waves.

a. Cyclotron-Wave Interaction

The dispersion relation (1) for the filled waveguide case may be reduced to a quadratic when roots close to $\beta_e + \beta_{ce}$ are sought. The assumptions required are:

$$\beta_z = \beta_e + \beta_{ce} + \Delta \tag{2}$$

$$\left(\frac{\Delta}{\beta_{ce}}\right)^2 \ll 1 \tag{3}$$

$$\omega \cong \omega_{ce}. \tag{4}$$

The resulting equation is

$$\left(\frac{\Delta}{\beta_{ce}}\right)^2 + \left(\frac{\Delta}{\beta_{ce}}\right)\left[\frac{1 - \left(\frac{\omega_{pp}}{\omega_{ce}}\right)^2 - \left(\frac{\omega_{pb}}{\omega_{ce}}\right)^2}{1 - \left(\frac{\omega_{pp}}{\omega_{ce}}\right)^2 + \left(\frac{\omega_{pb}}{\omega_{ce}}\right)^2} - \frac{1}{4}\frac{\left(\frac{\beta_T}{\beta_{ce}}\right)^2\left(\frac{\omega_{pp}}{\omega_{ce}}\right)^2}{\left(\left(\frac{\omega}{\omega_{ce}}\right)^2 - 1\right)\left(1 - \left(\frac{\omega_{pp}}{\omega_{ce}}\right)^2 + \left(\frac{\omega_{pb}}{\omega_{ce}}\right)^2\right)}\right]$$

$$- \frac{1}{8}\frac{\left(\frac{\omega_{pb}}{\omega_{ce}}\right)^2\left(\frac{\beta_T}{\beta_{ce}}\right)^2}{\left(1 - \left(\frac{\omega_{pp}}{\omega_{ce}}\right)^2 + \left(\frac{\omega_{pb}}{\omega_{ce}}\right)^2\right)} = 0 \tag{5}$$

For

$$\left(\frac{\omega}{\omega_{ce}}\right)^2 = 1 + \frac{1}{4}\frac{\left(\frac{\beta_T}{\beta_{ce}}\right)^2\left(\frac{\omega_{pp}}{\omega_{ce}}\right)^2}{1 - \left(\frac{\omega_{pp}}{\omega_{ce}}\right)^2 - \left(\frac{\omega_{pb}}{\omega_{ce}}\right)^2} \tag{6}$$

the "midband" coupling is given by

$$\left(\frac{\Delta}{\beta_{ce}}\right)^2 = \frac{1}{8}\frac{\left(\frac{\omega_{pb}}{\omega_{ce}}\right)^2\left(\frac{\beta_T}{\beta_{ce}}\right)^2}{1 - \left(\frac{\omega_{pp}}{\omega_{ce}}\right)^2 + \left(\frac{\omega_{pb}}{\omega_{ce}}\right)^2}. \tag{7}$$

According to the coupled-mode theory of backward-wave oscillators,[3] the starting length for oscillations is given by

$$L_o = \frac{1}{4}\frac{2\pi}{\Delta}. \tag{8}$$

The length is then seen to be inversely proportional to β_T and ω_{pb} within the assumptions of (2)-(4). For the partially filled tube, it is a good approximation to assume that

$J_o(\beta_T b) = 0$ to define β_T for the lowest order radial mode. For reasonable beam and plasma parameters, L_o is found to be approximately a few cyclotron wavelengths or less, and so this interaction might be expected to be observed in the laboratory.

b. Space-Charge Wave Interaction

The dispersion relation (1) is reduced to a cubic equation by seeking only roots close to β_e. Reduction to a quadratic equation is impossible because of the nearby fast space-charge wave. The assumptions involved are:

$$\beta_z = \beta_e + \Delta \tag{9}$$

$$\left(\frac{\Delta}{\beta_{ce}}\right)^2 \ll 1 \tag{10}$$

$$\omega \cong \omega_{ce}. \tag{11}$$

Only the filled-tube case will be considered here. The resulting cubic equation is

$$2\left(\frac{\Delta}{\beta_{ce}}\right)^3\left(1-\left(\frac{\omega_{pp}}{\omega_{ce}}\right)^2\right)+\left(\frac{\Delta}{\beta_{ce}}\right)^2\left[1-\left(\frac{\omega_{pp}}{\omega_{ce}}\right)^2-\left(\frac{\beta_T}{\beta_{ce}}\right)^2\left(\frac{\left(\frac{\omega_{pp}}{\omega_{ce}}\right)^2}{\left(\frac{\omega}{\omega_{ce}}\right)^2-1}+\left(\frac{\omega_{pb}}{\omega_{ce}}\right)^2\right)\right]$$

$$-2\frac{\Delta}{\beta_{ce}}\left(\frac{\omega_{pb}}{\omega_{ce}}\right)^2-\left(\frac{\omega_{pb}}{\omega_{ce}}\right)^2=0 \tag{12}$$

c. Power-Flow Analysis

To determine whether or not the system will oscillate, the electromagnetic power flow must be calculated as a function of distance. For backward-wave oscillations to take place, this power must flow in a direction opposite to that of the beam velocity at the point at which the beam enters the system; and it must vanish at some point along the interaction length. To analyze the power flow, the current, kinetic voltage, and longitudinal electric field are expressed as sums of waves characterized by the three wave numbers found from (12).

$$J(z) = J_1 e^{-j\beta_1 z} + J_2 e^{-j\beta_2 z} + J_3 e^{-j\beta_3 z} \tag{13}$$

$$U(z) = Z_1 J_1 e^{-j\beta_1 z} + Z_2 J_2 e^{-j\beta_2 z} + Z_3 J_3 e^{-j\beta_3 z} \tag{14}$$

$$E_z(z) = T_1 J_1 e^{-j\beta_1 z} + T_2 J_2 e^{-j\beta_2 z} + T_3 J_3 e^{-j\beta_3 z} . \tag{15}$$

The boundary conditions appropriate to a backward-wave oscillator are then applied at $z = 0$.

$$J(0) = 0 = J_1 + J_2 + J_3 \tag{16}$$

$$U(0) = 0 = Z_1 J_1 + Z_2 J_2 + Z_3 J_3 \tag{17}$$

$$E_z(0) = E_o = T_1 J_1 + T_2 J_2 + T_3 J_3 . \tag{18}$$

Equations 16-18 are solved for J_1, J_2, and J_3, and these quantities are used in evaluating the radial electric and azimuthal magnetic fields as functions of distance.

$$E_R(z) = S_1 J_1 e^{-j\beta_1 z} + S_2 J_2 e^{-j\beta_2 z} + S_3 J_3 e^{-j\beta_3 z}$$

$$H_\theta(z) = Q_1 J_1 e^{-j\beta_1 z} + Q_2 J_2 e^{-j\beta_2 z} + Q_3 J_3 e^{-j\beta_3 z} .$$

The values of Z_K, T_K, S_K, and Q_K can be found from the relations given by Smullin and Chorney.[4] Under the assumption that $\beta_{ce}^2 \gg (\beta_e - \beta_z)^2$, these values are:

$$Z_K = \frac{U_K}{J_K} = \frac{\beta_e - \beta_K}{\omega\epsilon_o \beta_{pb}^2} \tag{19}$$

$$T_K = \frac{E_{zK}}{J_K} = j \frac{(\beta_e - \beta_K)^2}{\omega\epsilon_o \beta_{pb}^2} \tag{20}$$

$$S_K = \frac{E_{rK}}{J_K} = -j \frac{\beta_T}{\beta_K} T_K \tag{21}$$

$$Q_K = \frac{H_{\theta K}}{J_K} = -\frac{\omega\epsilon_o \beta_K}{\beta_T^2} \left[1 - \left(\frac{\omega_{pp}}{\omega} \right)^2 - \frac{\beta_{pb}^2}{(\beta_e - \beta_z)^2} \frac{\beta_T^2}{\beta_e \beta_K} \right] S_K . \tag{22}$$

The coefficients (19)-(22) do not contain the radial dependence of the quantities in question, but only relate the multipliers of the appropriate Bessel functions. The J_o Bessel function is to be used with the current, kinetic voltage, and longitudinal electric field; and the J_1 Bessel function with the radial electric and azimuthal magnetic fields.

In the region of complex roots shown in Fig. II-7, the propagation constants may be written

$$\beta_1 = \beta_e - \beta_r + j\alpha \tag{23}$$

$$\beta_2 = \beta_e - \beta_r - j\alpha \tag{24}$$

$$\beta_3 = \beta_e + \beta_s \, . \tag{25}$$

The electromagnetic power density, normalized to $|P_3| = -S_3 Q_3 |J_3|^2$ is then found to be

$$\frac{\mathrm{Re}\left(E_R H_\theta^*\right)}{|P_3|} = -1 + \frac{\mathrm{Re}\left(S_2 Q_2 (J_2)^2\right)}{S_3 Q_3 |J_3|^2} - \frac{|J_2|^2}{|J_3|^2} \frac{\mathrm{Re}\left(S_2 Q_2^*\right)}{S_3 Q_3} \; 2 \cosh 2\alpha z$$

$$- \sinh \alpha z \sin (\beta_r + \beta_s) z \left[\frac{\mathrm{Re}\,(S_2 J_2)}{S_3 |J_3|} + \frac{\mathrm{Re}\,(Q_2 J_2)}{Q_3 |J_3|} \right]$$

$$+ 2 \cosh \alpha z \cos (\beta_r + \beta_s) z \left[\frac{\mathrm{Im}\,(S_2 J_2)}{S_3 |J_3|} + \frac{\mathrm{Im}\,(Q_2 J_2)}{Q_3 |J_3|} \right] . \tag{26}$$

To evaluate the total power flow, the power density must be integrated over the drift-tube cross section with the radial weighting function $J_1(\beta_T r)$, where $J_o(\beta_T a) = 0$

$$\mathrm{Re}\,(S_{em}) = \int_0^a \mathrm{Re}\left(E_R H_\theta^*\right) J_1^2(\beta_T r)\, 2\pi r \, dr \, . \tag{27}$$

The electromagnetic power vs distance has been computed throughout the range of complex roots shown in Fig. II-7. It is found that in each case, although the power flow at z = 0 is negative, at no point along the interaction distance does it become zero. A typical case is shown in Fig. II-8. Although the numerically computed dispersion curves were calculated for a weak beam, check calculations with $\omega_{pb}/\omega_{ce} = 0.1$ and 0.5 show the same behavior.

A clue to the reason for this behavior may be found in the real part of the complex propagation constants β_1 and β_2. Since β_r is positive, Re $(\beta_z) < \beta_e$ and the beam impedances Z_1 and Z_2 are positive. This means that the self-kinetic powers associated with waves 1 and 2 will be positive and the accompanying self-electromagnetic powers will be negative. These powers contribute the cosh 2αz turn to (26), which in each case investigated swamped out the other terms before the power flow had a chance to reach zero.

Figure II-8 shows that a backward-wave amplifier action occurs with a gain of

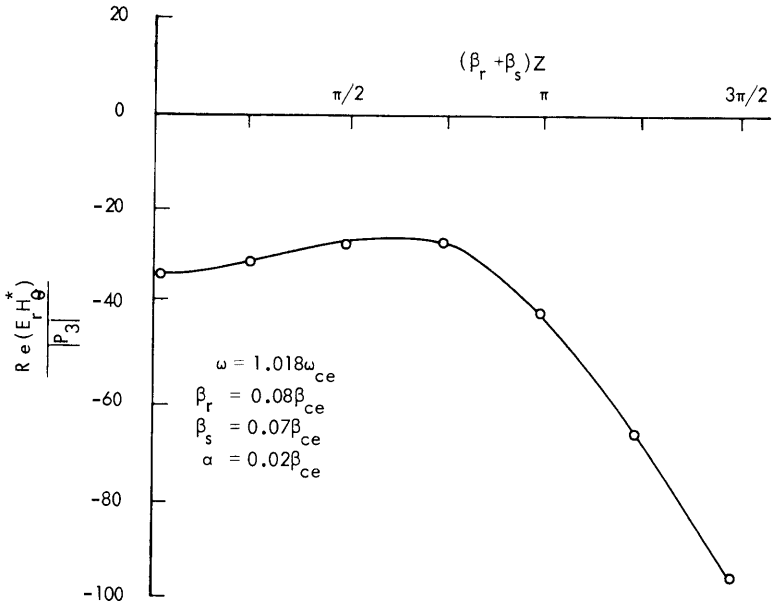

Fig. II-8. Normalized electromagnetic power flow vs distance.

approximately 1.3 at a length of 1.6 cyclotron wavelengths. The highest gain calculated was 4.5 at approximately 3.6 cyclotron wavelengths. If a system with reflecting end walls is considered, the possibility of oscillation once more exists. This question has yet to be investigated.

D. L. Morse

References

1. D. L. Morse, Plasma Heating by the Electron Beam-Plasma Interaction, S.M. Thesis, Department of Electrical Engineering, M.I.T., August 1961.

2. L. D. Smullin and P. Chorney, Propagation in Ion-Loaded Waveguides, Proc. Symposium on Electronic Waveguides, Polytechnic Institute of Brooklyn, New York, April 1958.

3. L. D. Smullin, Electron-Stimulated Ion Oscillations, Plasma Dynamics, Notes for Summer Session, M.I.T., 1959; see Chapter 5.

4. L. D. Smullin and P. Chorney, Propagation in Ion-Loaded Waveguides, op. cit.; see Appendix II.

5. AN ULTRAHIGH PERVIANCE ELECTRON GUN

The equation derived by Langmuir and Blodgett[1] for a space-charge-limited current between concentric spheres, which was adapted to gun design by J. R. Pierce,[2] does not contain any theoretical limitation on maximum perviance (perviance, $I/V^{3/2}$). However,

considerations of beam focusing and containment severely limit the maximum attainable perviance. For example, a spherically symmetric gun subtending a half-angle of 30° ceases to have focusing properties for a microperviance of 11.6. A possible way of alleviating this difficulty is to include ions for space-charge neutralization.

a. Design

A gun was designed to produce 10 amps of current 1000 volts; this is a microperviance of 316. The cathode was oxide-coated, subtending a half-angle of 60° and was heated from behind by electron bombardment. Cathode-to-screen radial ratio was 1.16.

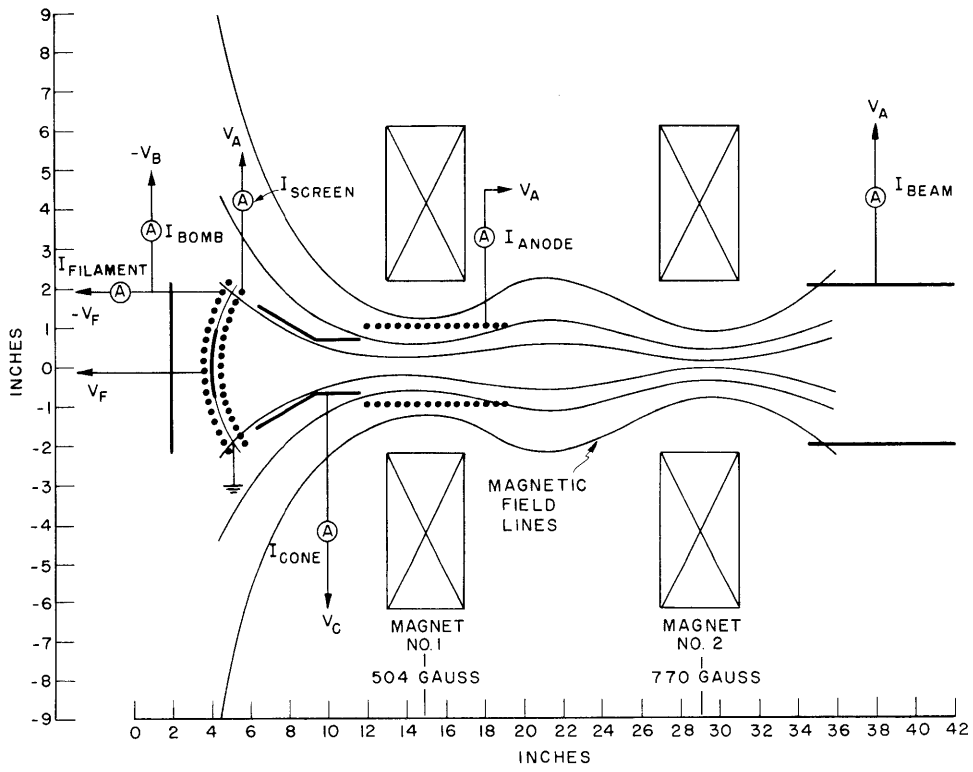

Fig. II-9. Ultrahigh perviance electron gun.

The ion trap was provided for by a cone-shaped electrode and an additional anode that was cylindrically shaped (see Fig. II-9). However, because of difficulties in heating and activating the cathode, the microperviance was reduced to approximately 84. This was accomplished by reducing the area of oxide coating on the cathode. For further design details see the author's thesis.[3]

b. Results

In the initial experiment, an electron beam having a microperviance of 61 was attained, at a voltage of 600 volts, and with a current of 900 ma. The microperviance of the sum of all of the currents was 82 and was sensitive to the cone voltage. When total current was plotted as a function of the ratio of cone-to-anode voltage (V_c/V_a) at V_a equal to 200 volts, there was a maximum microperviance of 85 at V_c/V_a equal to 0.66. However, in the initial experiment only fixed ratios of V_c/V_a were attainable, and the beam current of 900 ma at 600 volts is probably not the maximum obtainable.

It was also found that proper operation depended on the background pressure and on high ratios of V_c/V_a. When the background pressure was lower than 1×10^{-5} mm Hg the obtainable beam currents were less than 10 ma. An uncontrolled arc discharge with currents in excess of 10 amps developed for background pressures in excess of 4×10^{-5} mm Hg, or for high values of V_c/V_a with V_a greater than 200 volts. The exact values of V_c/V_a at which this occurs was not determined. In was found, however, to be dependent on the anode voltage V_a. A possible explanation of this behavior can be found by looking at the equation for the shielding distance of a plasma,

$$\lambda_e \propto (T_e/n_e)^{1/2}$$

where T_e is the temperature of the electrons released in ionizing collisions of the background gas with the beam electrons. These secondary electrons will be accelerated and trapped between the cathode and cone, in the region of the accelerating screen. T_e will then be highly dependent on $V_a - V_c$. The density, n_e, of these trapped electrons will depend directly on background pressure and anode voltage, and indirectly on several loss mechanisms.

When T_e and n_e are such that the shielding distance becomes less than the distance between the accelerating screen wires, the electric fields are no longer of the form for which the gun was designed and an arc discharge develops.

c. Conclusions

It has been shown that electron beam currents are obtainable, from a Pierce design, of an order of magnitude greater with the use of ions than can be obtained without their use. More experimental work is required to determine all of the operating characteristics.

R. J. Pellar

References

1. L. Langmuir and K. Blodgett, Currents limited by space charge between concentric spheres, Phys. Rev. 24, 49-59 (1924).

2. J. R. Pierce, Theory and Design of Electron Beams (D. Van Nostrand Company, New York, 1954).

3. R. J. Pellar, An Electron Gun of Moderate Voltage High Current Capabilities, S. B. Thesis, Department of Physics, M. I. T., June 1961.

6. THE MAGNETIC PUMP – A DEVICE FOR THE MECHANICAL GENERATION OF HIGH MAGNETIC FIELDS

It has been realized for some time that the ability of a superconducting loop to maintain a constant magnetic flux through its boundaries offers a method for the "direct" conversion of mechanical to magnetic energy. Consider, for example, the situation diagramed in Fig. II-10 in which two superconducting loops are in such close proximity as to link essentially the same total magnetic flux.

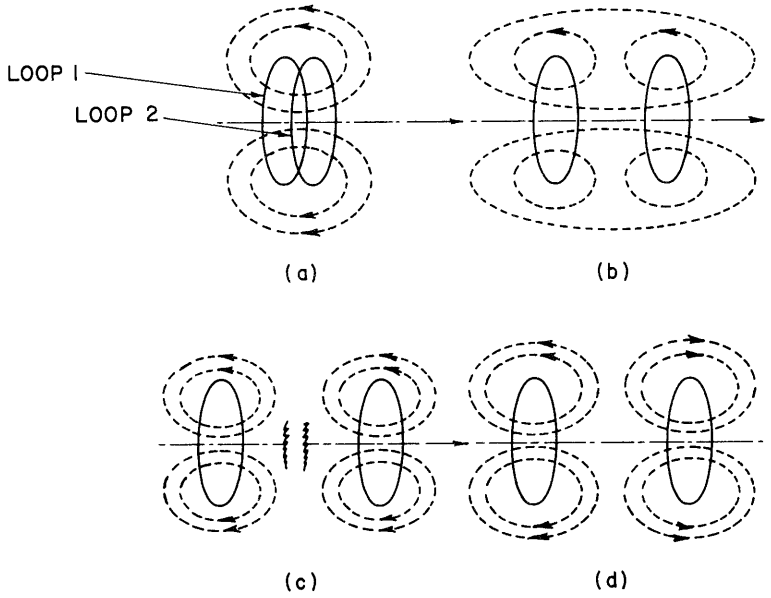

Fig. II-10. Separation and rotation of superconducting loops.

If loop 2, while still superconducting, is pulled out along the symmetry axis, a situation will eventually ensue wherein there are two independent loops, each carrying the same circulating electric current as the sum of the currents in the original pair, and each producing a magnetic field identical to the original field. Note that the total magnetic-field energy has been doubled (at the expense of work done in separating the loops), but the magnetic-field strength is nowhere higher than it is in the starting configuration. If loop 2 is now rotated 180° about one of its diameters and pushed back

toward the origin, the total magnetic-field energy is further increased, but the flux through each of the loops is still identical to that in the starting configuration. The same final configuration can be obtained by rotation of one coil shown in Fig. II-10a without translation, and the same amount of work is involved.

At present, it appears more desirable to achieve higher field strengths at a given point than simply to increase the total magnetic-field energy in the universe. The former aim requires an increase in magnetic flux through any given loop. Several devices have been discovered which, operating in a cycle, will do just that.

Figure II-11 shows an operating cycle of one of these devices consisting of six square loops of superconducting material arranged in a cubic array. Loops 5 and 6 remain superconducting at all times and serve as flux barriers. Loops 1, 2, 3, and 4 may be switched between superconducting and normal states, and, furthermore, loops 3 and 4 are movable. The first half-cycle is illustrated in Fig. II-11b. Loop 1 is linked by a total flux of 1 unit, and loops 2 and 4 contain no total flux. Loop 3 in the normal (or open-circuited) state is pushed into close proximity with loop 1 and then

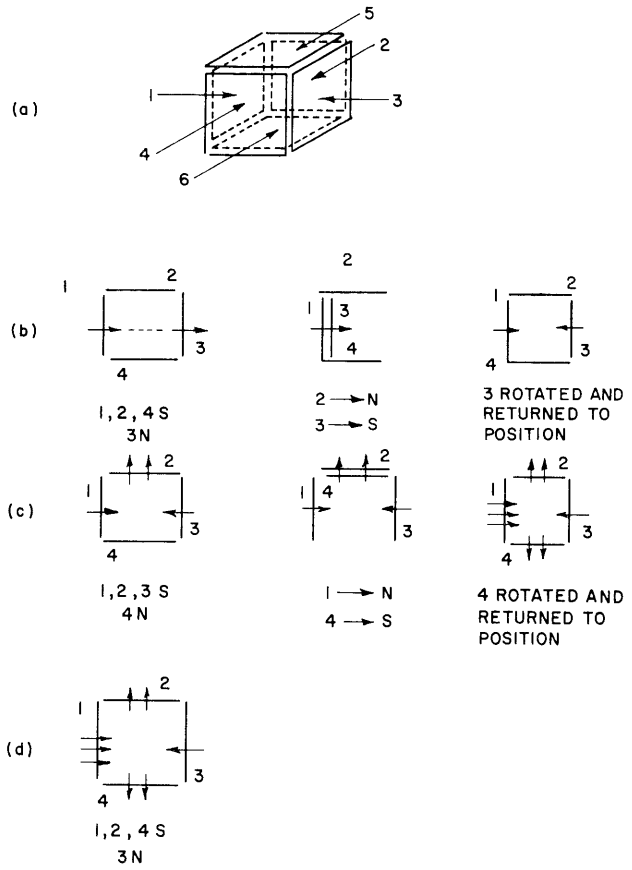

Fig. II-11. Cubic configuration cycle of magnetic-field pump.

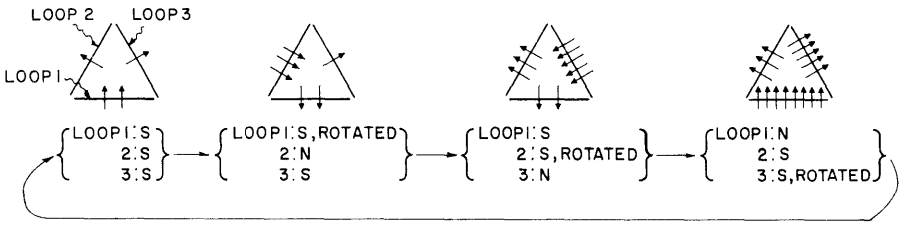

Fig. II-12. Prism configuration cycle of magnetic-field pump.

switched to the superconducting (S) state. Loop 2 is, at this time, switched to the normal (N) state. Loop 3 is then rotated through 180° and returned to its original position. A total of 2 units of flux must now pass through loop 2. In Fig. II-11c the second half-cycle is performed with loop 4 as the moving element. This leads to the configuration of Fig. II-11d, which is identical to that of Fig. II-11b, except that the flux through all loops has been increased. The cycle may now be repeated.

Figure II-12 illustrates a complete cycle in the operation of a somewhat more sophisticated design. This magnetic pump consists of 5 loops arranged in the form of a triangular prism with the base loops, 4 and 5, serving as flux barriers. The cycle begins with 2 units of flux through loop 1, and 1 unit through each of loops 2 and 3. As the first step in the cycle, loop 2 is either open-circuited or switched to the normal state and loop 1 rotated through 180°. Three units of flux must then pass through loop 2. The cycle continues in the same direction, eventually returning to the original configuration but with increased flux through all of the loops.

Both of these schemes are subject to the obvious limits imposed by the critical currents and fields of the superconducting material used and the somewhat less obvious problems of flux leakage between loops and resistive losses in normal material at the time of flux changes. Of the last two, the first may be minimized by proper mechanical design, and the second by either open-circuiting all normal loops or operating as slowly as is practical.

This general method for the increase of magnetic fields becomes of interest when it is considered for use in conjunction with the recently developed "hard" superconductors. Magnetic pumping should allow the attainment of very high sheet currents in a superconducting solenoid without recourse either to many turn coils or high-current electrical generators with the attendant heat leaks of large volumes of good electrical (and thermal) conductors.

D. J. Rose, L. M. Lidsky, R. C. Wingerson

7. TWO-METER PLASMA EXPERIMENT

The variant of the hollow-cathode-discharge plasma source described here was specifically designed to furnish a dense ($10^{13}/cm^3$), highly ionized (≥ 50 per cent) plasma

for studies of plasma acceleration by moving magnetic fields. Toward this end, a linear system was built with a plasma source at one end, an easily accessible "acceleration region" in the center, and flight space for analysis of the accelerated plasma at the opposite end. Inasmuch as the plasma generated is 5-10 cm in diameter and 2 m long – that is, suitable for such things as long-arc or wave-propagation studies – the design was kept as flexible and unspecialized as possible.

Figure II-13 is a simplified schematic diagram illustrating the positions of the major components of the device and the layout of the pumping system. Electrical connections, cooling provisions, access port locations, safety interlocks, and so forth, have been omitted from the drawing. The basic electrical system is similarly abstracted in

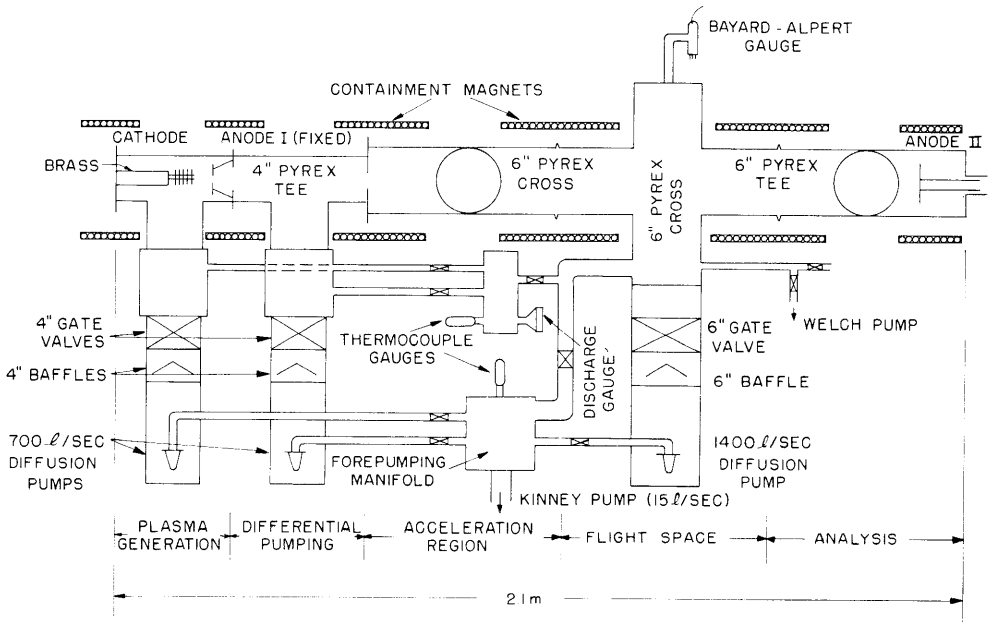

Fig. II-13. Schematic diagram of major components.

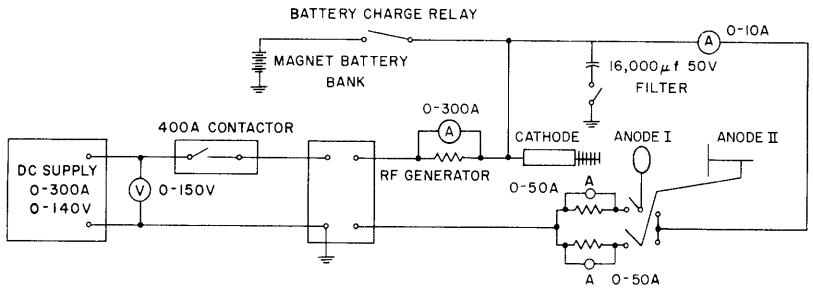

Fig. II-14. Simplified schematic diagram of main electrical circuitry.

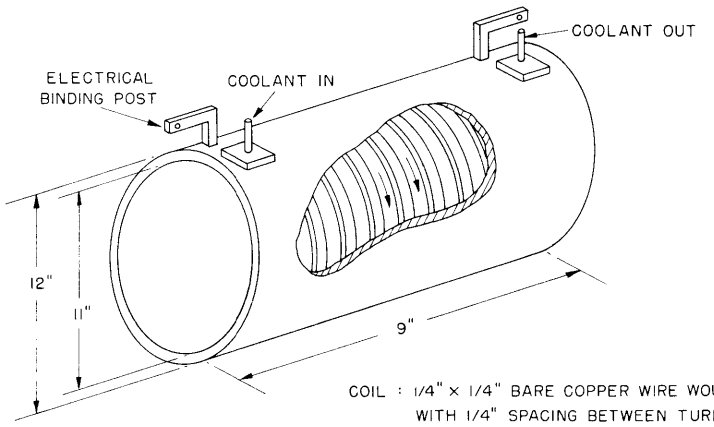

COIL : 1/4" × 1/4" BARE COPPER WIRE WOUND WITH 1/4" SPACING BETWEEN TURNS

CASING : 1/8" SHEET PVC

COOLING : TOP WATER FLOWING SPIRAL PATH BETWEEN TURNS

RESISTANCE : ≈ 0.01 Ω

MAXIMUM CURRENT = > 450A

(a)

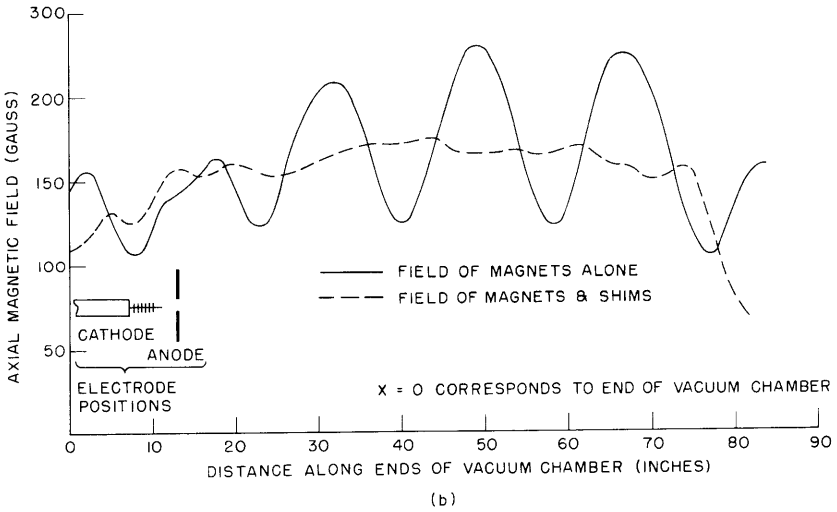

(b)

Fig. II-15. (a) Containment magnet design. (b) Effect of shims on axial containment field.

Fig. II-14. Note that the discharge may be made to occur either across or along the axial magnetic field. In the usual case, movable anode II is completely withdrawn from the vacuum chamber. The containment magnets (Fig. II-15a) can furnish a nearly uniform axial field of more than 400 gauss over the 2-m length of the system. They are of somewhat unusual design because of spatial limitations imposed by the connecting flanges needed between sections of the glass vacuum chamber. The design achieves light weight, small size, ease of construction and operation at the cost of a very low Fabry factor. All magnets are lined with sheet iron shims to furnish a more uniform field. Figure II-15b demonstrates the utility of this method of achieving field uniformity while preserving simple construction and ease of access. Figure II-16 is a more detailed view of the plasma-generation chamber. It is very similar in electrode configuration to the hollow-cathode discharge in the reflex configuration described heretofore, and the operating parameters (current, voltage, pressure, gas input rate, etc.) are roughly the same as those described in previous reports.[1,2]

Although the plasma generator was designed to be used in conjunction with a still unfinished plasma accelerator, it is quite well suited for experiments of other kinds. It has been used for this purpose while the accelerator is under construction. One of these experiments, conducted to take advantage of the invariance of discharge parameters to

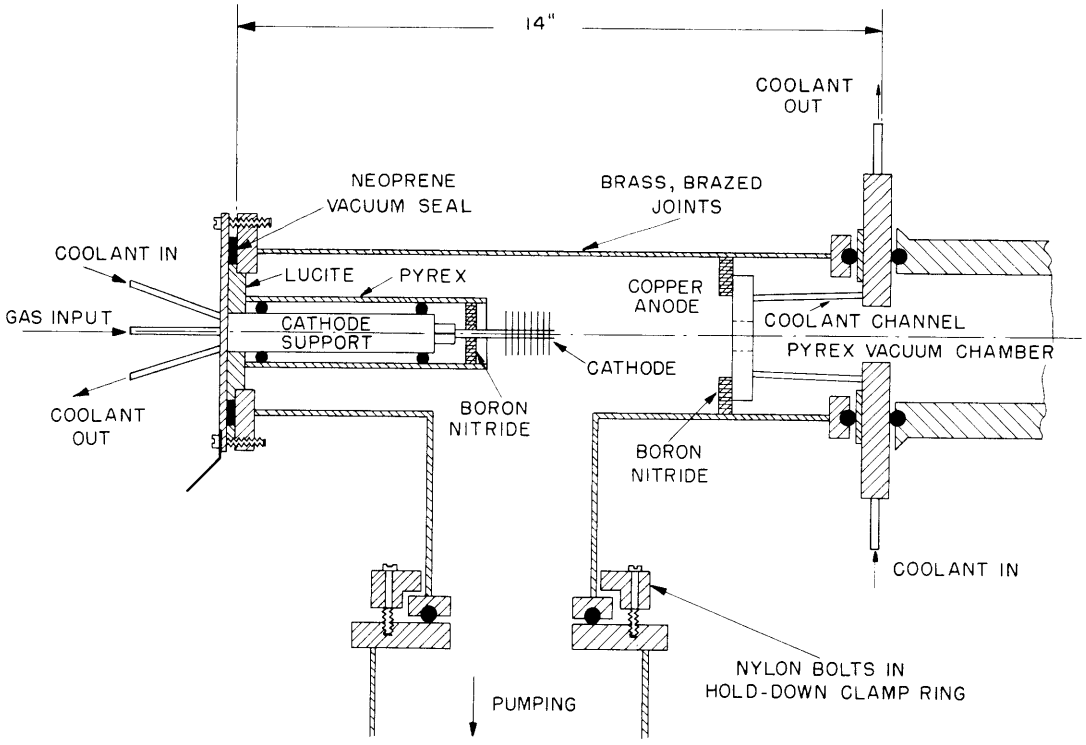

Fig. II-16. Plasma generation chamber.

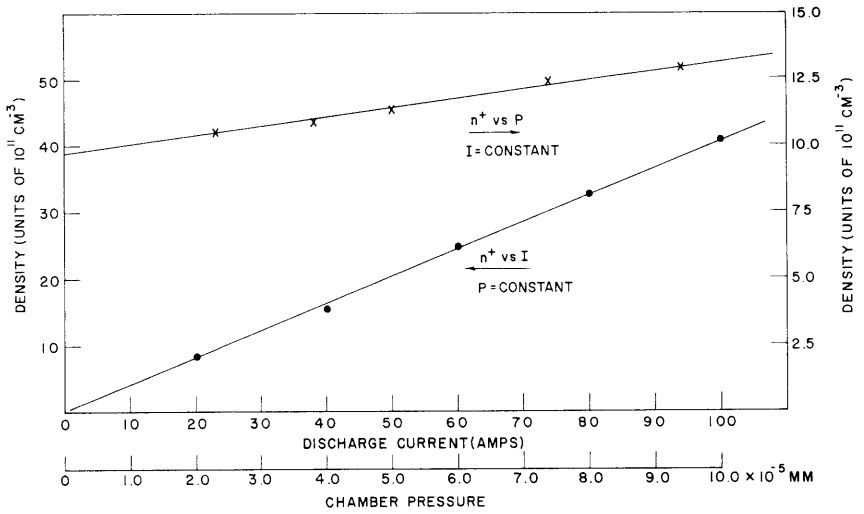

Fig. II-17. Dependence of charge density on discharge current and chamber pressure.

conditions in the experimental portion of the system, indicates that the plasma is indeed formed in the interior of the hollow cathode and not as the result of external ionization. The pressure was varied by controlling the opening of the 6-inch gate valve; pressure was measured by a Bayard-Alpert gauge, and plasma density by a Langmuir probe. The results, plotted in Fig. II-17, were obtained in two different runs because of the limitation of working time set by discharge of the containment magnet battery bank. It is clear, however, that the plasma density is only slightly dependent on neutral gas pressure. Extrapolation of both curves to zero pressure and current lend credence to the hypothesis that secondary ionization is of secondary importance. The linear dependence of plasma density on discharge current illustrated in Fig. II-17 is exhibited in all experiments. The slope of this line is a strong function of input gas feed rate and axial magnetic field.

Table II-2. Identification of brightest spectral lines.

Source	Number
AI	23
AII	125
Ta	4
Undetermined	3

Spectroscopic studies in which a Jarrell-Ashe J8000 monochrometer was used were carried out at the same spatial location. The 155 brightest lines between 3000 Å and

5000 Å wavelength were identified with the results presented in Table II-2. Lack of knowledge of excitation cross sections and transition probabilities precludes quantitative analysis of these data, but the general picture is that of a highly ionized, high-purity plasma. The variation of brightness of several AI and AII lines as a function of discharge current is shown in Fig. II-18. The argon II intensity increases more rapidly than the first power of current; this indicates that the ionized argon already present is

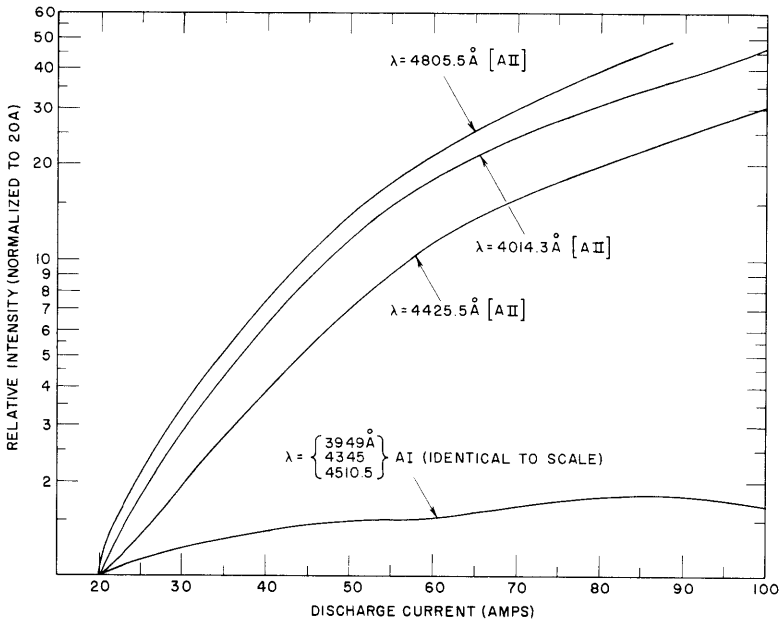

Fig. II-18. Intensity variation of selected spectral lines as a function of discharge current.

being excited by the streaming electrons in the central core. The neutral argon spectral intensity increases more slowly than the first power of discharge current; this indicates that the major source of neutral argon spectra lies outside the main body of the plasma. Behavior of these lines at high current appears to demonstrate "burnout" of the neutral argon.

A "floating" electrostatic probe inserted into the plasma will exhibit, under certain broad conditions of plasma density and temperature, well-defined electrical oscillations of 1-5 volts magnitude at frequencies of 5-50 kc. The frequency of these oscillations immediately brought to mind the observation of standing ionic sound waves at Oak Ridge National Laboratory.[3] To test this hypothesis, an experiment was performed in which plasma density, temperature, and oscillation frequency were simultaneously measured by a Langmuir probe. Oscillograms of the oscillations are reproduced in Fig. II-19, and the reduced data in Table II-3 and Fig. II-20. Note that the oscillation period does

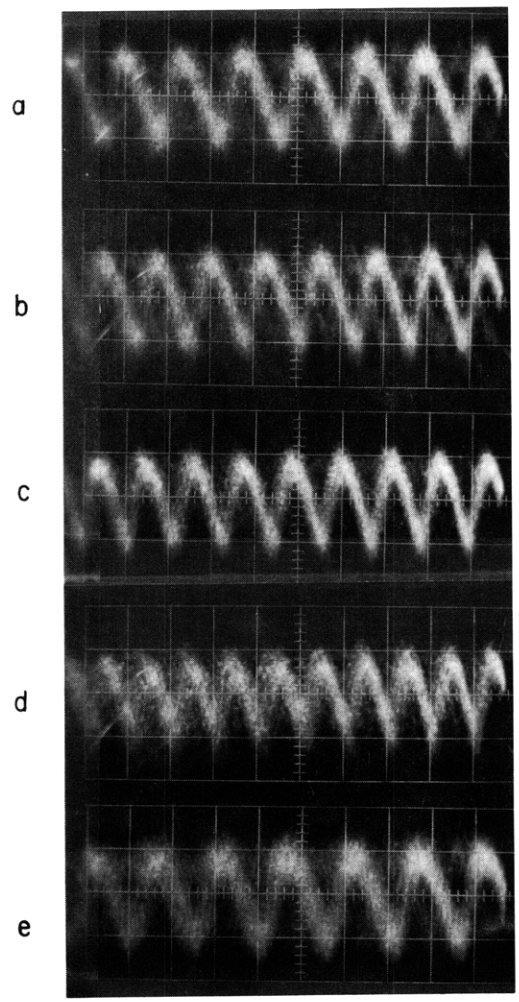

Fig. II-19. Signal on "floating" probe (vertical, 2 volts/cm; sweep, 0.1 msec/cm).

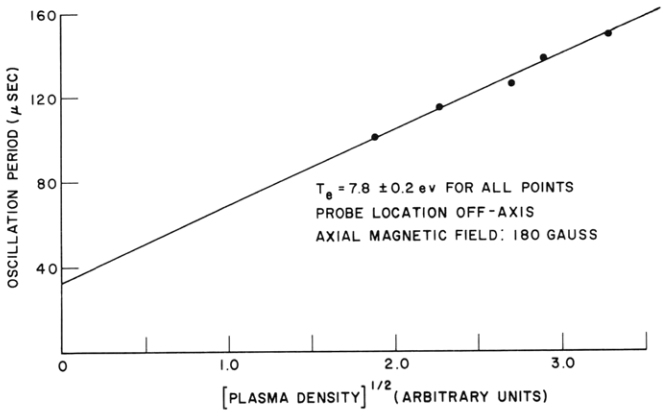

Fig. II-20. Oscillation frequency as a function of plasma density.

Table II-3. Plasma properties and oscillation period data. (cf. Fig. II-19.)

Discharge Current (amps)	Plasma Density	Plasma Temperature (ev)	Trace*	Oscillation Period (τ) (μsec)
20	$3.59 \times 10^{11}/cm^3$	7.96	d	100
30	5.16	7.66	c	114
40	7.30	7.69	b	126
50	8.40	7.94	a	139
62	10.7	7.78	e	149

*See Fig. II-19.

not depend on plasma temperature (as it would for sound waves) but does vary linearly with $n^{1/2}$ (as it would for Alfvèn waves). The frequency is found to be a strong function of the axial B field and slightly dependent on the length of the plasma column. However, the plasma density is also strongly dependent on the axial field, and a separation of magnetic field and plasma density effects has been postponed until the installation of a continuously variable, steady power source for the containment magnets.

Several modifications are being made. Chief among these are the installation of a 500 amp, 40 VDC welding power supply to replace the battery bank, and a change in anode design to one that will permit the use of large apertures. On the basis of past work, this last change should permit the generation of significantly hotter, denser plasmas.

The traveling-wave acceleration is predicated on the use of a very high dielectric constant ceramic cylinder that will serve as the dielectric in a continuously distributed loaded line. An analysis of this accelerator will appear in subsequent reports.

L. M. Lidsky

References

1. W. D. Getty, A low-pressure gas-arc device, Quarterly Progress Report No. 57, Research Laboratory of Electronics, M.I.T., April 15, 1960, pp. 27-29.

2. W. D. Getty and L. D. Smullin, Experimental results of the study of the hollow-cathode discharge, Quarterly Progress Report No. 58, Research Laboratory of Electronics, M.I.T., July 15, 1960, pp. 35-41.

3. I. Alexeff and R. V. Neidigh, Observation of Ionic Sound Waves in Gaseous Discharge Tubes, ORNL Report Central File No. 61-6-66, Oak Ridge National Laboratory, 1961.

8. HELICAL RESONANT-BEAM TRAPPING

In recent months we have developed an analytical solution for the "resonant corkscrew,"[1] a properly designed modified helical magnetic-field source.[2] Based on equations from this analysis, design and preliminary construction work have been initiated to verify the analytical solution and to yield information for which the use of the analytical solution would be too tedious and costly.

The equations that were used in the design are:

$$p(z) = -\frac{2\pi m V_z(z)}{qB_o}$$

where p is the corkscrew pitch, m is the electron mass, B_o is the axial field, V_z is the axial velocity, and q is the electron charge.

$$\left(\frac{qB_o}{m}\right)\frac{V_\perp(z)}{z} = \beta(z)\left[I_o\left(\frac{2\pi m V_\perp(z)}{qB_o p(z)}\right) + I_2\left(\frac{2\pi m V_\perp(z)}{qB_o p(z)}\right)\right]$$

where $V_\perp$ is the transverse velocity, $\beta(z)$ is the transverse component of the field on axis, and the conservation of energy is given by

$$V_\perp^2 + V_z^2 = V_o^2$$

where V_o is the initial velocity (axial). Five approximations are implicit in these equations: pitch and transverse field strength vary slowly (helix is modified only slightly); only the lowest eigenfunctions are used in the field expression (valid for certain corkscrew configurations and ratios of corkscrew radius to cyclotron radius); the particle guiding center is on axis; the particle transverse velocity is always at right angles to the transverse field component; and the particle trajectory is approximately a helix.

These design criteria allow one of the design variables, p(z), V(z), β, B_o, to be arbitrarily specified. The easiest approach was to specify the pitch, and the dependence chosen was $p(z) = 1 + b \sin^4\left(\frac{\pi 2}{\ell}\right)$. The use of this function restricts the range of the variation of the ratio of the corkscrew radius to the cyclotron radius, if the best transverse field distribution is to be obtained.

Because of the approximations that the corkscrew pitch and field are slowly varying, it is essential that the ratio of the corkscrew length to its radius should be large in order to justify the use of the design equations. For the planned experiment, the axial field will be provided by an 8-ft solenoidal magnet with a maximum field strength of 800 gauss; the usable portion of which, for the corkscrew to be in a constant field, is 82 inches.

To determine the corkscrew radius, the design equations yield a value for

the end velocity of

$$\frac{V_z(L)}{V_o} = \frac{1}{1+b}.$$

For the initial experiment, it was decided to put 75 per cent of the axial energy into the transverse component. This energy transfer occurs for b = 1. The function chosen for the pitch variation gives the best transverse field distribution for a ratio of corkscrew radius to cyclotron radius of approximately 3.5. The system was tuned to receive 2-kv electrons into a constant axial field of 210 gauss. This arrangement yielded a corkscrew diameter of 2 inches and a ratio of corkscrew length to radius of 82. It is hoped that this ratio is large enough to satisfy the slow-change approximation, and an experimental measurement of the field is to be conducted to verify this fact.

Figure II-21 shows curves of the design parameters for this electron corkscrew. The corkscrew structure providing the perturbing field is a quadrafilar winding that enables the field to be adjusted so as to vary smoothly. In this arrangement two of the wires carry current in a direction opposite to the other two, and this cancellation allows the field to go to zero at both ends, while the field strength along the corkscrew is adjusted by a separation angle between pairs of wires.

With a vacuum system pressure of approximately 10^{-7} mm Hg, it is hoped that the optimization of the corkscrew will allow a containment time of approximately 1000 transits. This containment time will be one of the major parameters to be measured. The dependence of the containment time on the fine tuning of the system will be checked by adjusting all variables.

Mirrors, capable of 2 kgauss, will be available at either end of the system to contain the wound-up particles and to provide a maximum mirror ratio of approximately 10. A better understanding of the first-order scatter will be available from the data obtained by varying the mirror ratio and observing the distribution leaving the bottle. By means of a properly biased Faraday collector, the outcoming current can be measured and the energy distribution will be found.

The use of bellows will allow the phase and off-axis position of the entering particle to be adjusted, and information on the criticalness of such factors will be yielded.

Since the expected containment time of 1000 traversals is not long enough for a thermonuclear experiment, a larger containment time is necessary. One method of achieving a greater containment time is to have resonant molecules dissociate, so that the resulting atomic particles are affected only to second order by the corkscrew. This molecular break-up containment will be investigated by the use of two 4-ft corkscrews, the first of which will be tuned to the entering particles, and the second to a particle with twice the velocity. Winding the electron with only the first tuned corkscrew activated, and then switching to the second untuned corkscrew, is mathematically equivalent

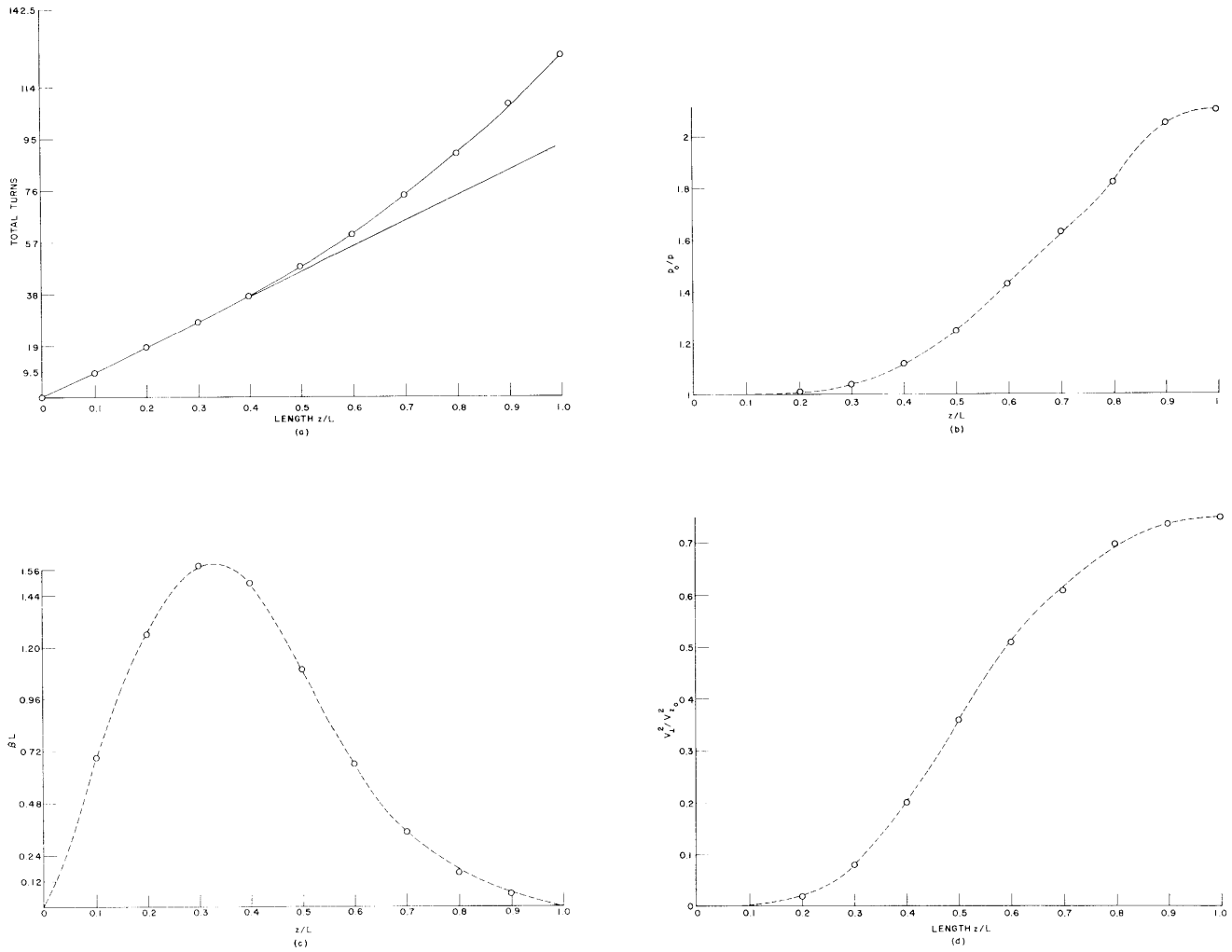

Fig. II-21. Theoretical design parameters plotted as a function of corkscrew distance. (a) Total number of helical turns. (b) Size of pitch length. (c) Shape of transverse field on axis. (d) Transverse velocity.

to the molecular breakup of a hydrogen molecule. This experiment will allow observation of the second-order resonance effect which cannot easily be calculated.

The operation of this electron corkscrew should yield a large amount of information about the general usefulness of this particular means of injection into a magnetic bottle.

D. J. Rose, R. C. Wingerson, J. S. Tulenko

References

1. R. C. Wingerson, Electron beam trapping, Quarterly Progress Report No. 60, Research Laboratory of Electronics, M.I.T., January 15, 1961, pp. 59-65.

2. R. C. Wingerson, Non-Adiabatic Motion of Charged Particles in Corkscrew Magnetic Field, Ph.D. Thesis, Department of Nuclear Engineering, M.I.T., February 1961.

9. SUPERCONDUCTING NIOBIUM-TIN SOLENOID

A Nb_3Sn superconducting solenoid generating 28.5 kgauss has been constructed. A sketch of the magnet is found in Fig. II-22. Three separate windings were used. The two reasons for this configuration were: the increase of quenching current with decreasing magnetic field permitted high currents in the outer section; and more

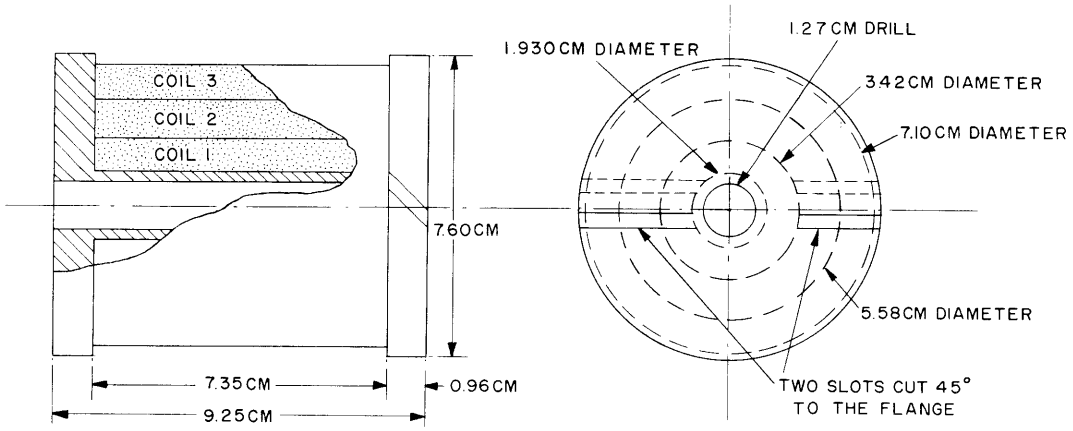

Fig. II-22. 304 stainless-steel coil form and windings for the large solenoid.

versatility was obtained in the event that a poor section of wire limited the current-carrying ability of any single winding. Preliminary to the construction of the large solenoid, several smaller ones were constructed to explore the materials and design parameters that were to be used for the large solenoid. These small solenoids generated from 6.9 kgauss to 10.4 kgauss. A sketch of the mounting form for these coils is shown in Fig. II-23. The extension tube to the coils served to support the long leads that are

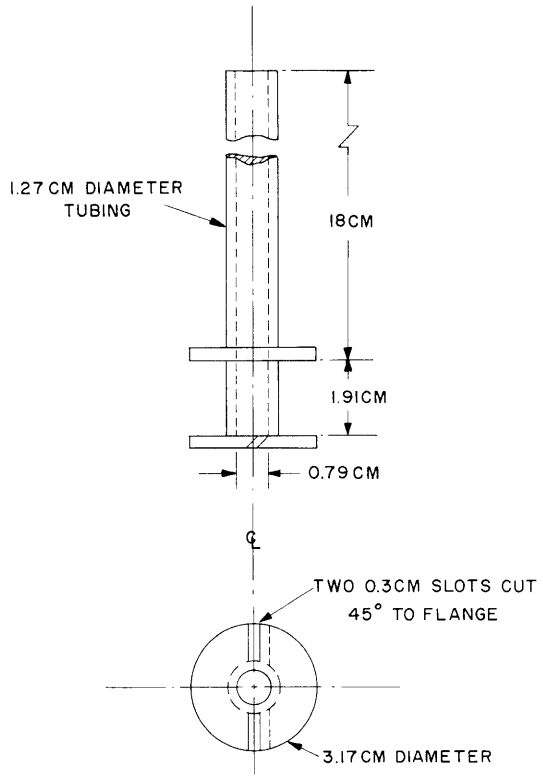

Fig. II-23. 304 stainless-steel spool and support tube for small coils.

required to remove the contacts between the superconducting wire and the regular Cu wire from the external test field of the Bitter magnet.

a. Design Problems

The design problems encountered were: (a) the superconducting wire, (b) materials for the supporting coil mandrel, (c) insulation of the superconducting wire and mandrel, (d) potting the windings, (e) support and protection of the leads against shearing, and (f) making contacts to the normally conducting current leads. Discussion of these problems follows.

(i) The Nb_3Sn intermetallic compound (from National Research Corporation) was unreacted powder, as a 0.010-inch core in a hollow 0.020-inch diameter Nb wire. This formed a strong means of support for the fragile Nb_3Sn. This wire had to be heat-treated (950°C for 16 hours) to react the powder core and form Nb_3Sn. The Nb:Nb_3Sn wire could not be bent after the heat treatment, as such work would fracture the core. This limitation meant that the wire had to be wound before heating, and required that the coil form and insulation be compatible with the wire during the heat treatment.

(ii) Type 304 stainless steel was used for the coil form and for the tubing supporting

the superconducting leads. Compatibility tests indicated that any adverse effect on the wire caused by the stainless steel was obscured by inconsistencies in the superconducting wire itself. Attempts were made to use Mo spools mounted on a quartz support tube, but thermal stresses and relative motions generated upon cooling to liquid nitrogen temperatures resulted in shearing the leads to the windings.

(iii) A commercially available insulation, capable of withstanding the reacting temperature, was found: "Ceron F," employed by the Sprague Electric Company at their plant in Bennington, Vermont. Their insulating process consisted of electrophoretically coating the wire with a ceramic in solution, followed by protective binder, and baking at 500°C to 800°C. The binder would evaporate upon heating to the 950°C temperature used to form the Nb_3Sn. The ceramic contained ZnO, Talc, China Clay, and sodium silicate. The binder was undisclosed. This insulation added only 0.8 mils to the diameter of the wire. Although the insulation would withstand the abrasions of winding the coil, any rubbing against the stainless-steel form would result in a short circuit. Sauereisen Cement No. 1 was applied as a thin coat to the stainless-steel form to insulate it.

(iv) The Sauereisen cement was found compatible with the Nb:Nb_3Sn wire and was also used to pot the windings. Such potting is necessary to prevent any detrimental movement of the wire caused by magnetic forces. This cement worked well for the small test coils, but gave trouble during the heat treatment of the large solenoid. Steam formed from water held by the cement forced its way out of the coil. The water was either left in the cement from inadequate curing or was absorbed from the atmosphere. The steam forcing through the windings rearranged the insulation, leaving the coil badly shorted. The short circuits were of high resistance and were not superconducting.

(v) Support of the superconducting leads from the coil proved troublesome. It was necessary to allow the wire some freedom of movement because a rigid attachment to the wire would cause it to shear. Teflon spaghetti was run onto the wire and taped to the support tube with Teflon tape.

(vi) Contacts between the Nb:Nb_3Sn wire and the Cu current leads were made by plating Cu on the end of the superconducting lead. The end was tinned with Cd-Sn solder and joined to the Cu wire with rosin core solder. This gave a good, easily disassembled junction.

b. Tests

The small coils were tested under their own fields and in the 10-cm, 66.5 kgauss Bitter magnet. The large coil was tested under its own field. All tests were performed at 4.2°K. The results of the small coils are presented in Table II-4. Coils 1 and 2 were not tested in the Bitter magnet because their leads sheared. The results of the tests of coils 3 and 4 in the Bitter magnet are presented in Fig. II-24. The poorer

Table II-4. Results of small-coil tests.

Small Coil Number	Length of Wire (meters)	Quench Current (amps)	Self-field Generated (kgauss)
1	13.7	60	7
2	13.4	82	10
3	4.7	88	6.9
		106 (11.7 kgauss external fields)	8.4
4	9.6	80	10.2

Table II-5. Performance of the large solenoid, individual windings.

Winding	Quenching Current (amps)	Calculated Field (kgauss)	Experimental Field (kgauss)	Ratio of Experimental to Calculated Field
1	51	15.6	15.0	0.96
2	52	18.8	16.5	0.88
3	34	8.0	5.7	0.67

Table II-6. Performance of the large solenoid, all windings.

Coil Amperage				Calculated Field (kgauss)	Experimental Field (kgauss)	Ratio of Experimental to Calculated Field
Winding	1	2	3			
1	35	51	0	29.2	25.9	0.89
2	39	45	0	28.2	26.4	0.94
3	34	45	20	29.6	28.5	0.96
4	30	40	25	29.5	28.2	0.96

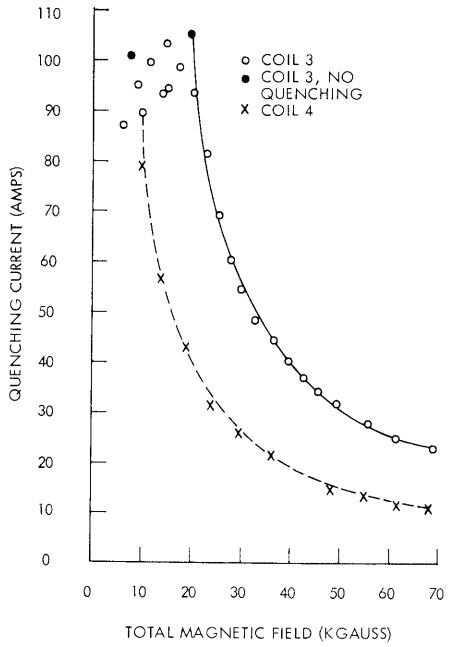

Fig. II-24. Results of high-field tests of coils 3 and 4.

results of coil 4 could be explained by some oxidation of the wire during the heat treatment upon the loss of the inert helium atmosphere.

The results of the tests for the individual windings for the large solenoid are presented in Table II-5, while those for the windings run together are found in Table II-6. The current-carrying ability of this solenoid is poorer than that of the small coils. This behavior probably arises from the trouble encountered during the heat treatment, but it may also arise from variations in the superconducting wire itself, which would show up in long lengths but not in short ones.

L. C. Salter, Jr., D. J. Rose

II-C. PLASMA MAGNETOHYDRODYNAMICS AND ENERGY CONVERSION*

Prof. E. N. Carabateas
Prof. J. A. Fay
Prof. G. N. Hatsopoulos
Prof. W. D. Jackson
Prof. H. P. Meissner
Prof. D. C. Pridmore-Brown
Prof. A. H. Shapiro
Prof. H. H. Woodson
L. Y. Cooper
R. S. Cooper
D. M. Dix
D. A. East
W. H. Heiser
E. D. Hoag
F. D. Ketterer
S. A. Khayatt
G. B. Kliman
P. Klimowski
A. Kniazzeh
M. F. Koskinen
A. T. Lewis
J. R. Melcher
W. T. Norris
E. S. Pierson
J. W. Poduska
J. H. Wasserlein
G. L. Wilson

1. PARAMETRIC GENERATOR

Suggestions have been made that the energy carried by a pulsating flow of ionized gas can be extracted by allowing the gas to traverse a coil, thereby periodically varying the inductance parameter of the coil. If losses are low enough and if the coil is tuned with a capacitance,[1-4] self-excitation can occur.

Some highly idealized analyses have been made to determine some criteria for self-excitation[3] and to determine some limits on performance.[4] Thus far, no detailed description of the behavior of such a generator is available because the time- and space-dependent magnetohydrodynamic problem involved is extremely complex, and relevant plasma experiments are difficult to perform.

Our present purpose is to report on experiments with a system in which solid conductors are used to traverse a coil and vary the inductance. Such a system should behave like a plasma system except for compressibility effects. Therefore some conclusions can be drawn about how well previous idealized analyses describe parametric generator operation, and about the relations between static ac properties of the conductor-coil system and the generator with relative motion between conductor and coil.

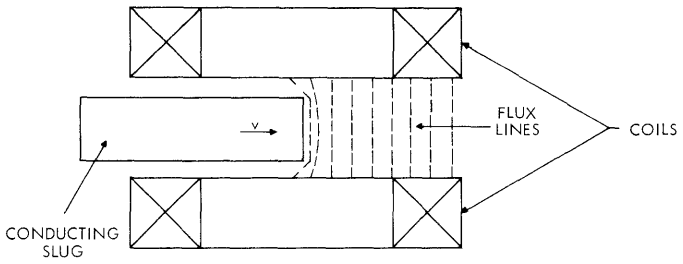

Fig. II-25. Displacement of flux lines by the conducting slug.

*This work was supported in part by National Science Foundation under Grant G-9330, and in part by WADD Contract AF33(616)-7624 with Flight Accessories Laboratory, Wright-Patterson Air Force Base, Ohio.

a. Theory

When conducting slugs periodically traverse the coils as shown in Fig. II-25, with a radian frequency 2ω, the reciprocal inductance of the series-aiding coils can be written approximately as

$$\Gamma(t) = \Gamma_o + \Delta\Gamma \sin 2\omega t. \tag{1}$$

If small losses are assumed, the winding resistance can be treated near resonance as a shunt conductance, and the equivalent circuit of Fig. II-26 results, in which G_e

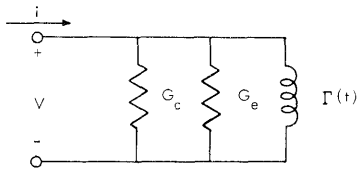

Fig. II-26. Equivalent circuit.

represents eddy current losses in the conducting slugs, and G_c represents winding losses and is given by

$$G_c = \frac{\Gamma_o^2 R}{\omega^2}, \tag{2}$$

where R is the winding resistance.

Excitation of the system of Fig. II-26 by a voltage source,

$$v(t) = V \sin(\omega t - \phi), \tag{3}$$

yields the current

$$i(t) = -\frac{\Gamma_o V}{\omega}\cos(\omega t-\phi) - \frac{\Delta\Gamma V}{2\omega}\cos 2\phi \sin(\omega t-\phi) - \frac{\Delta\Gamma V}{2\omega}\sin 2\phi \cos(\omega t-\phi)$$

$$- \frac{\Delta\Gamma V}{2\omega}\sin(3\omega t-\phi) + (G_c+G_e)\, V \sin(\omega t-\phi). \tag{4}$$

Equations 3 and 4 can be used to construct the modified equivalent circuit of Fig. II-27, in which the conductance G_p is given by

$$G_p = -\frac{\Delta\Gamma}{2\omega}\cos 2\phi. \tag{5}$$

This conductance can be negative, so if the system is tuned by a capacitance given by

$$C = \frac{\Gamma_o}{\omega^2}, \tag{6}$$

if a low-impedance shunt path is provided for the third-harmonic current, and if

$$G_{p\,max} = -\frac{\Delta\Gamma}{2\omega} = G_c + G_e, \tag{7}$$

then the system will operate in the steady state with no electrical excitation source and will be self-excited. When the negative conductance G_p is larger than (G_c+G_e) the

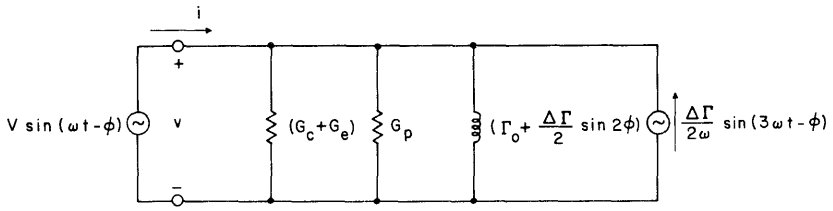

Fig. II-27. Modified equivalent circuit.

system is unstable and the current and voltage amplitudes will grow exponentially until something in the system becomes nonlinear. From these considerations, it is evident that the criterion for self-excitation[4] is

$$-\frac{\Delta\Gamma}{2\omega} \geq G_c + G_e. \tag{8}$$

Although direct measurements can be made and scaling laws can be derived, it is much easier to make calculations and measurements on a stationary, steady-state ac system. Consequently, a comparison will be made between results calculated from steady-state ac test data and results obtained from the operating parametric system.

In the experiment described below self-excitation was not achieved; however, it is evident from Eqs. 3 and 4 and from Fig. II-27 that the size and character of the conductance G_p can be studied by varying the phase angle (ϕ) of the electrical excitation with respect to the phase of the inductance variation and measuring the impedance.

b. Experiment

The experimental arrangement of coils and copper slugs is shown in Fig. II-28. The radius of the bakelite disc was determined by the size of an installed drive motor and by mechanical stress limitations. The axial length of the system was determined by steady-state ac measurements to obtain the maximum fractional change in inductance with the coils shown in Fig. II-28. The two coils wound with No. 20 Formvar magnet wire, which are connected series-aiding in the geometry of Fig. II-28, have a resistance of 14.7 ohms and a maximum inductance of 65 mh.

The circuit of Fig. II-29 was used to obtain the steady-state ac data of Table II-7.

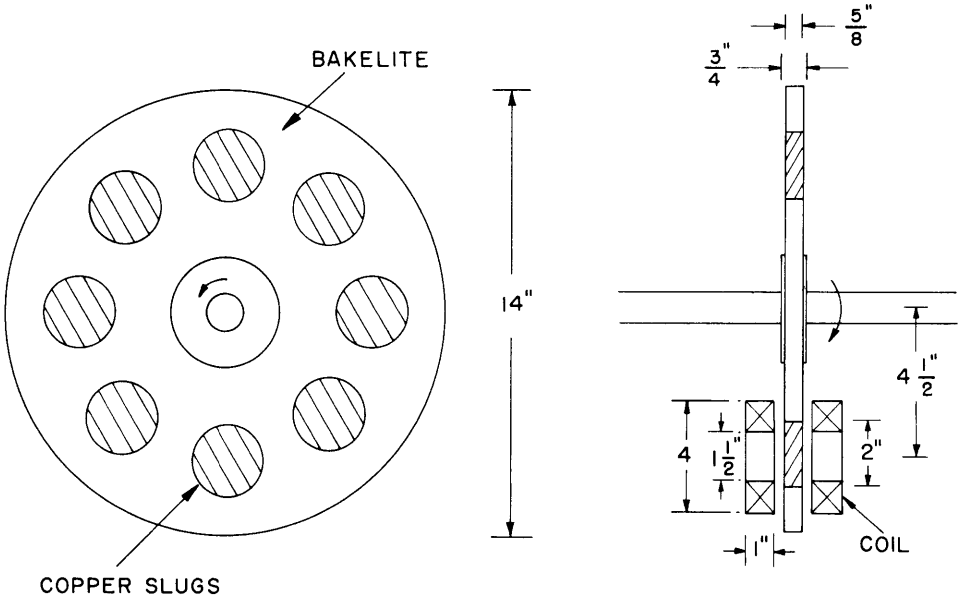

Fig. II-28. Two views of wheel with position of coils shown in end view of the wheel.

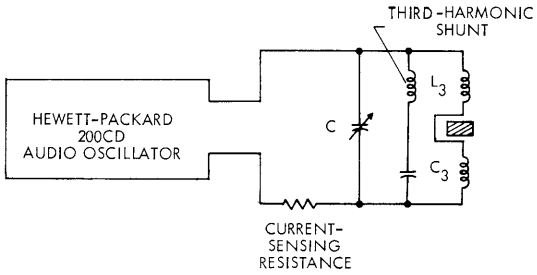

Fig. II-29. Circuit for steady-state ac measurements.

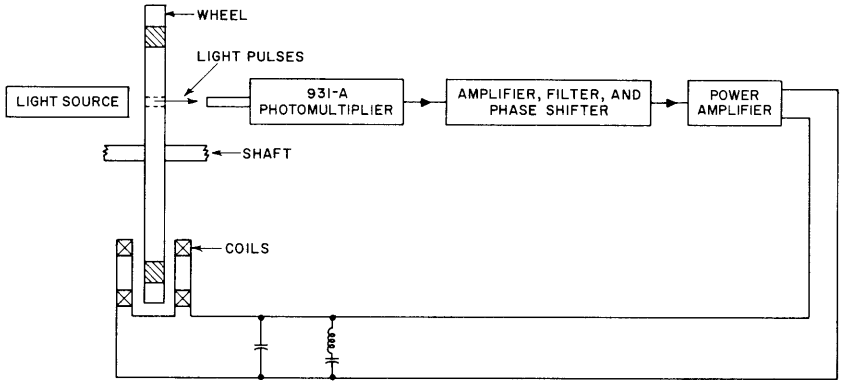

Fig. II-30. System for negative-conductance measurements.

Table II-7. Steady-state ac measurements.

Frequency (cps)	Slug between Coils		Slug out of Coils		Γ_o (h^{-1})	$\Delta\Gamma$ (h^{-1})	G_c (mhos)	G_e (mhos)
	Γ_{max} (h^{-1})	G_{max} (mhos)	Γ_{min} (h^{-1})	G_{min} (mhos)				
200	5.9	$.86 \times 10^{-3}$	5.3	$.52 \times 10^{-3}$	5.6	.3	$.52 \times 10^{-3}$	$.34 \times 10^{-3}$
250	6.0	$.61 \times 10^{-3}$	5.4	$.35 \times 10^{-3}$	5.7	.3	$.35 \times 10^{-3}$	$.26 \times 10^{-3}$
300	6.1	$.42 \times 10^{-3}$	5.5	$.26 \times 10^{-3}$	5.8	.3	$.26 \times 10^{-3}$	$.16 \times 10^{-3}$

All measurements were made on a calibrated oscilloscope at resonance, reached by tuning capacitor C. The quantities in the first four columns of Table II-7 were measured directly, and the remaining quantities were obtained from the expressions,

$$\Gamma_o = \frac{\Gamma_{max} + \Gamma_{min}}{2}; \quad \Delta\Gamma = \frac{\Gamma_{max} - \Gamma_{min}}{2};$$
$$G_c = G_{min}; \qquad G_e = G_{max} - G_{min}. \tag{9}$$

For the highest speed at which the wheel can be driven, the system losses are too great for self-excitation. Consequently, to investigate the negative conductance predicted by Eq. 5, excitation is necessary at half the frequency at which the slugs traverse the coils and with variable phase. This excitation is provided by a system shown in block diagram form in Fig. II-30. Light pulses are obtained through four equally spaced holes in the bakelite wheel. These light pulses excite a photomultiplier whose output is

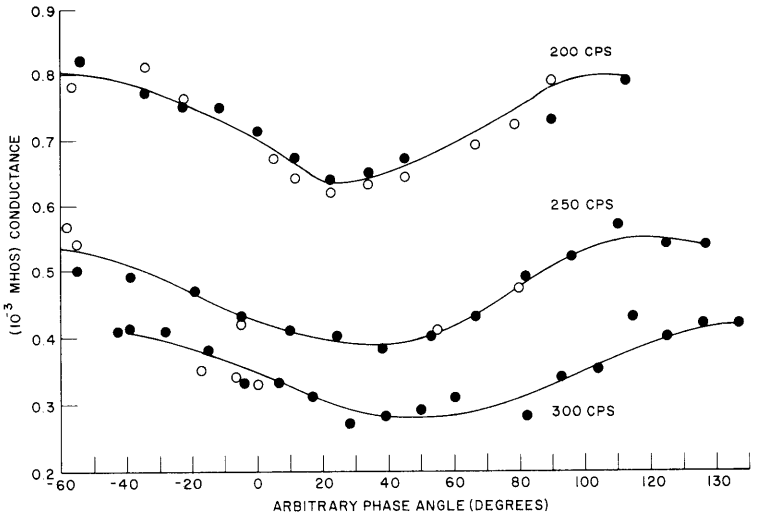

Fig. II-31. Conductance vs excitation phase angle.

amplified and filtered to obtain the fundamental frequency component. This signal is fed to a phase shifter and then into a power amplifier that excites the tuned circuit. Best results (the least harmonics) were obtained when the excitation source had much higher internal impedance than the third-harmonic shunt circuit, so that the excitation appeared as a current source.

The experimental results of conductance measurements are plotted for three different rotational speeds in Fig. II-31. The phase angle is measured from an arbitrary reference. The shape of the curves are approximately sinusoidal, as predicted by Eq. 5, enabling the measurement of conductance change with phase angle.

Table II-8. Compilation of results.

Frequency (cps)	Experimental Results with Wheel Driven Mechanically			Theoretical Predictions with Steady-State ac Measurements		
	Gc + Ge (mhos)	$G_{p\ max}$ (mhos)	H	Gc + Ge (mhos)	$G_p = -\frac{\Delta\Gamma}{2\omega}$ (mhos)	H
200	$.72 \times 10^{-3}$	$.08 \times 10^{-3}$	.11	$.86 \times 10^{-3}$	$.12 \times 10^{-3}$	.14
250	$.47 \times 10^{-3}$	$.08 \times 10^{-3}$	.17	$.61 \times 10^{-3}$	$.10 \times 10^{-3}$	.16
300	$.35 \times 10^{-3}$	$.07 \times 10^{-3}$	.20	$.42 \times 10^{-3}$	$.08 \times 10^{-3}$	.19

Theoretical and experimental results are shown for comparison in Table II-8. Equation 8, the condition for self-excitation, is rewritten as

$$H = \frac{\Delta\Gamma}{2\omega(G_c+G_e)} = \frac{G_{p\ max}}{G_c + G_e} \geq 1. \tag{10}$$

This parameter as shown in Table II-8 indicates that self-excitation cannot occur because of the losses in the system. However, the results indicate good correlation between steady-state ac measurements and direct measurements on the parametric system.

c. Conclusions

The good agreement between parameters calculated from the results of steady-state ac measurements and parameters measured directly in the parametric system indicates that steady-state analysis of a static ac system may be sufficient to predict the performance of a parametric generator. This approach is markedly simpler than an attempt to solve the time-dependent magnetohydrodynamic problem.

This simple experiment provides a good analytical and experimental basis on which to predict accurately the conditions under which a parametric generator can be self-excited, and to predict the performance characteristics of a self-excited generator.

Although these measurements were made on a system of rigid conductors, the results are still applicable to a system of gaseous conductors. The results are directly applicable to the prediction of self-excitation in the gaseous system and will become inaccurate only for large signals when the gaseous conductor begins to deform appreciably.

H. H. Woodson, G. L. Wilson, M. Smith

References

1. S. A. Colgate, and R. L. Aamodt, Plasma reactor promises direct electric power, Nucleonics 15, 50 (1957).

2. M. V. Clauser, Magnetohydrodynamics, in Space Technology, edited by H. S. Siefert (John Wiley and Sons, Inc., New York, 1959), Chapter 18.

3. H. H. Woodson and W. D. Jackson (eds.), Summary Report: Study of Electrical Energy Conversion Systems for Future Aircraft, WADD Technical Report 60-148, Electronic Systems Laboratory, M. I. T., February 1960, pp. 67-89.

4. H. H. Woodson and A. T. Lewis, Some requirements for the operation of magnetohydrodynamic induction generators, Proc. Second Symposium on the Engineering Aspects of Magnetohydrodynamics, Power Conversion Session (Columbia University Press, New York, 1961).

2. EXPERIMENTAL STUDY OF THE OSCILLATIONS OBSERVED IN CESIUM THERMIONIC CONVERTERS

A thermionic converter operating at low cesium pressure so that the cesium mean-free path is considerably larger than the interelectrode spacing exhibits oscillations in its electrical output. Such oscillations have been reported for both plane[1, 2] and cylindrical configurations.[3] The measurements reported have been mainly conducted with a resistive load, and therefore during a cycle both the current output and the difference in Fermi levels of emitter and collector change with time. To obtain an insight into the exact mechanism of these oscillations, three devices were constructed having cylindrical copper collectors with diameters of 0.250 inch, 0.312 inch, and 0.625 inch. All collectors had a length-to-diameter ratio of 2, and all devices used 0.0125-inch diameter niobium wire as an emitter. The emitter was heated by half-wave-rectified 60-cycle current, and the output was observed on an oscilloscope during the period in which no heating current was passing through the emitter.

Oscillations were observed with three different types of load: resistive, constant-current, and constant-voltage. The frequency of oscillations under resistive load at a

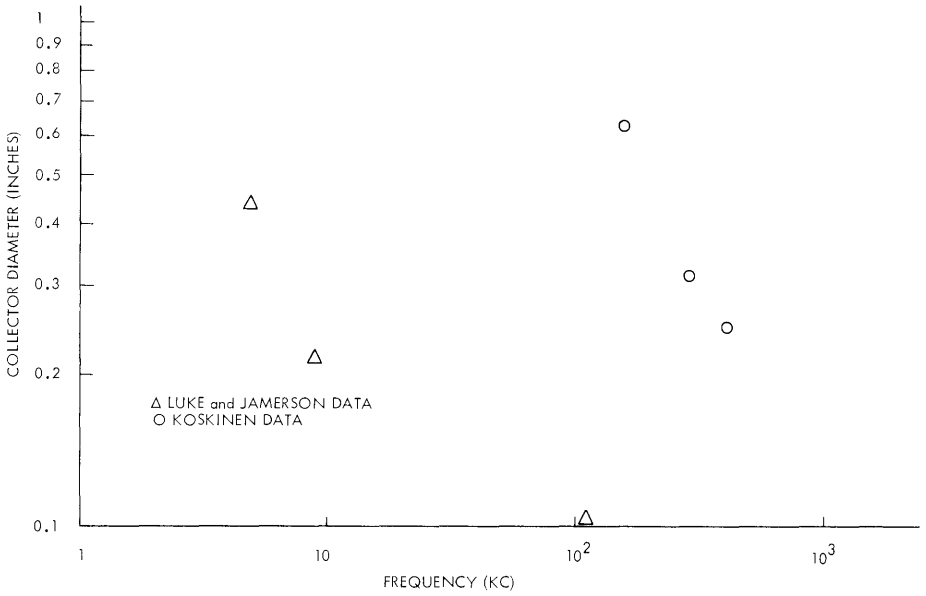

Fig. II-32. Oscillation frequency at various collector diameters.

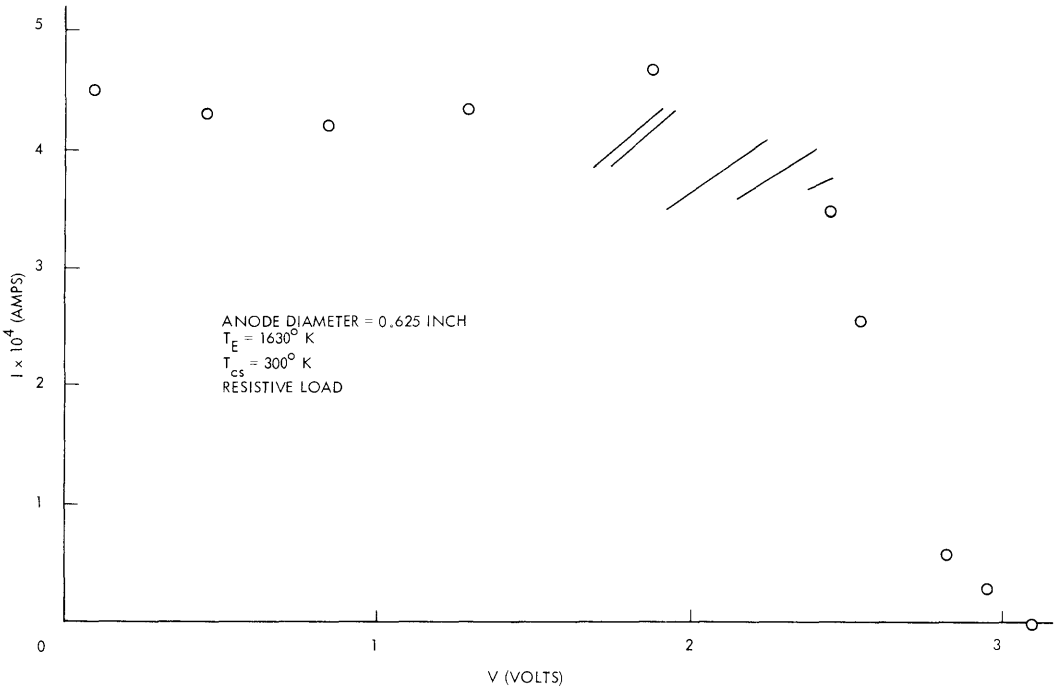

Fig. II-33. I-V curve with resistive load showing oscillations.

cesium bath temperature of 300°K is shown in Fig. II-32 for the three different collector diameters. These data seem to indicate that oscillation frequency is inversely proportional to the collector diameter. On the same figure the experimental data reported by Luke and Jamerson[3] for a cesium bath temperature of 473°K are also shown.

More extensive testing has been performed on the 0.625-inch diameter collector unit. Under a resistive load oscillations only occurred at the knee of the I-V curve (Fig. II-33) and in a narrow range of emitter temperatures (1680-1700°K). Figures II-34,

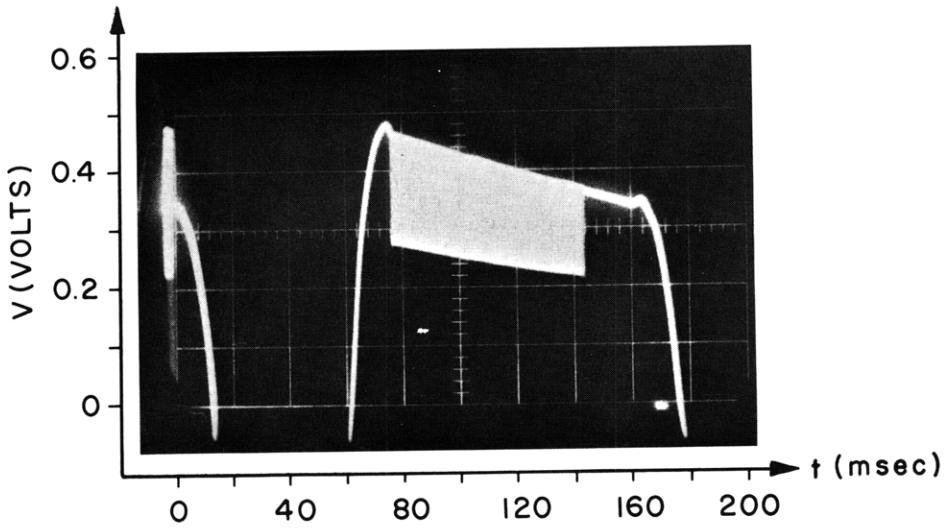

Fig. II-34. Voltage vs time, resistive load, T_E = 1680°K, T_{cs} = 300°K.

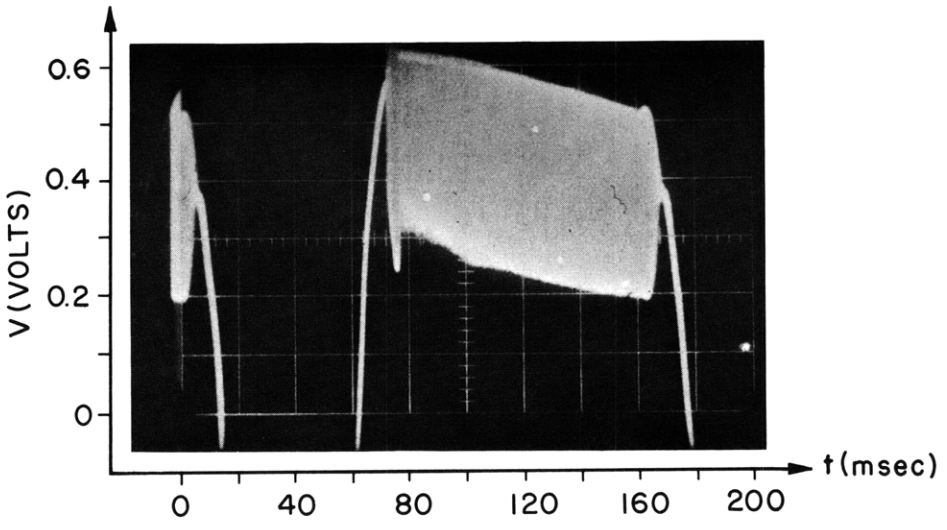

Fig. II-35. Voltage vs time, resistive load, T_E = 1690°K, T_{cs} = 300°K.

II-35, and II-36 show oscilloscope traces of the output voltage at 1680°K, 1690°K, and 1700°K. The first part of the trace is the emitter heating period, followed by the observation period, which is characterized by a decline in output voltage with time that apparently is due to the fact that the filament temperature decreases with time. Figures II-34 and II-36 are especially interesting, as one can observe oscillations starting and stopping as the emitter temperature is varied. It is also interesting to note that the oscillations are not centered on the dc level, but are surges to lower outputs. The oscillation

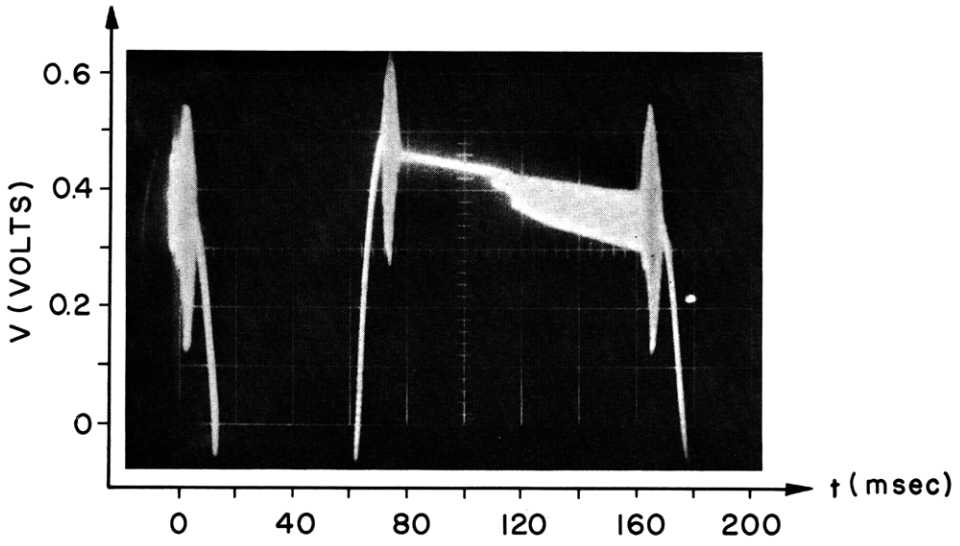

Fig. II-36. Voltage vs time, resistive load, T_E = 1700°K, T_{cs} = 300°K.

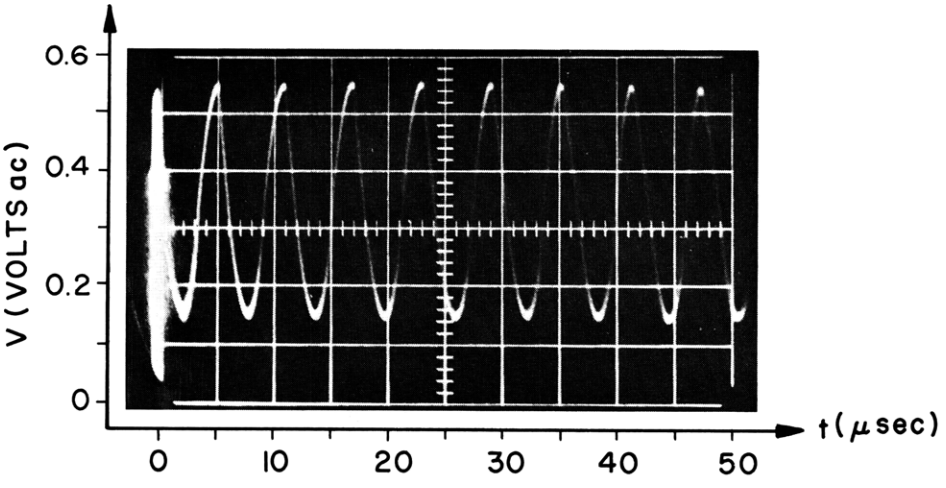

Fig. II-37. AC component of voltage vs time, resistive load, T_E = 1690°K, T_{cs} = 300°K.

waveform is shown in Fig. II-37. Experiments with a resistive load carried out on the 0.250-inch diameter collector are shown in Fig. II-38, in which the frequency of oscillation is plotted as a function of cesium bath temperature. Above 410°K the oscillations disappear.

Oscillations under constant current load appear only in the constant-current portion of the I-V curve as shown in Fig. II-39. The frequency of oscillation is the same as it is with resistive load. They also exhibit the same surging toward low output as the oscillations under resistive load.

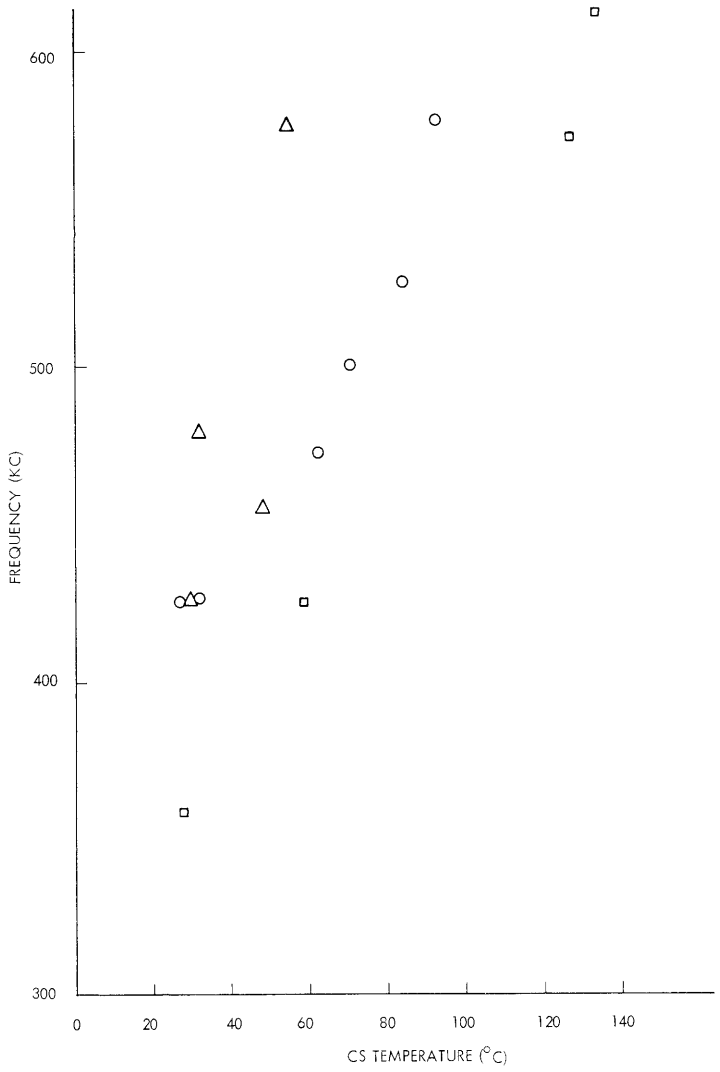

Fig. II-38. Oscillation frequency at various cesium bath temperatures. The emitter temperature was adjusted at every point for maximum oscillation amplitude. The three sets of points shown in this figure are for three different runs.

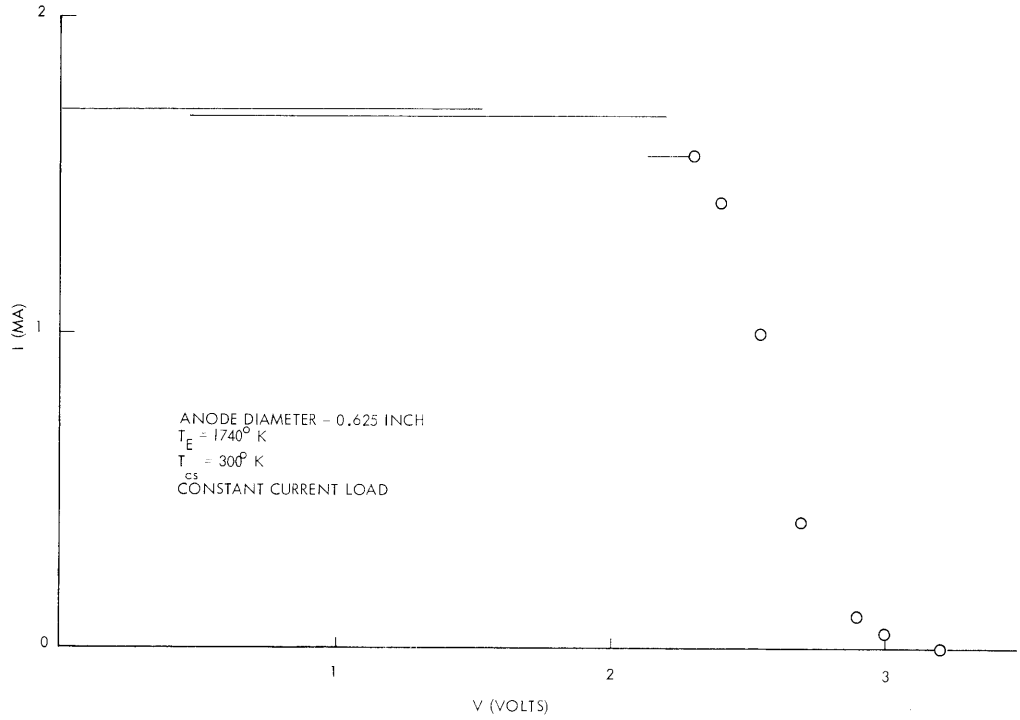

Fig. II-39. I-V curve with constant-current load showing oscillations.

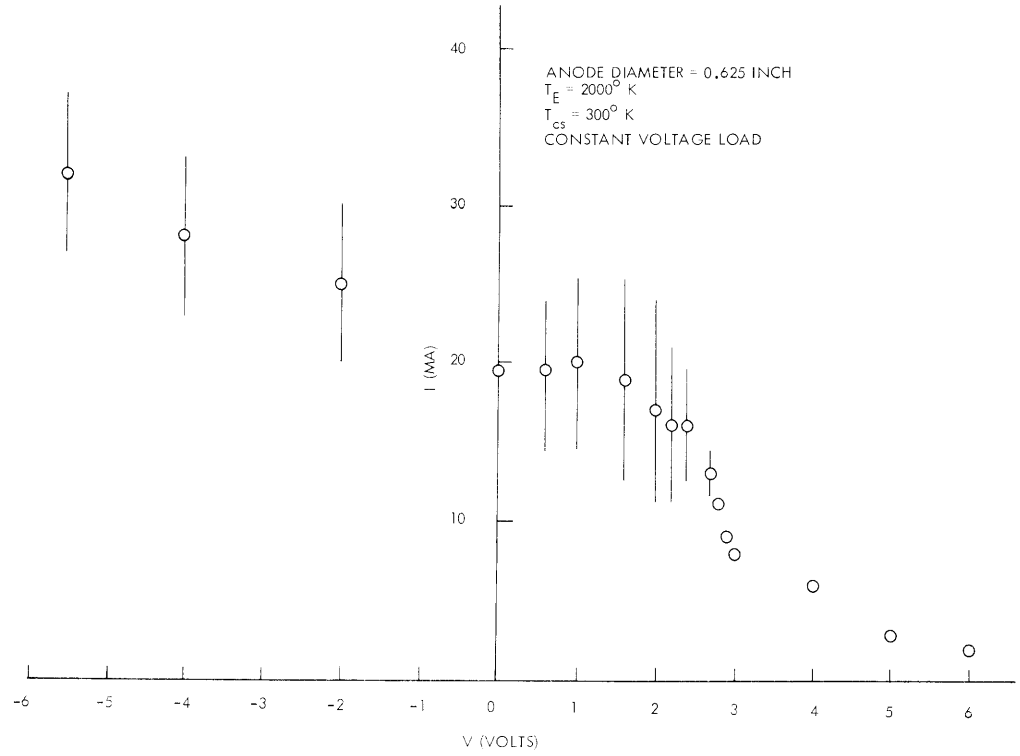

Fig. II-40. I-V curve with constant-voltage load showing oscillations.

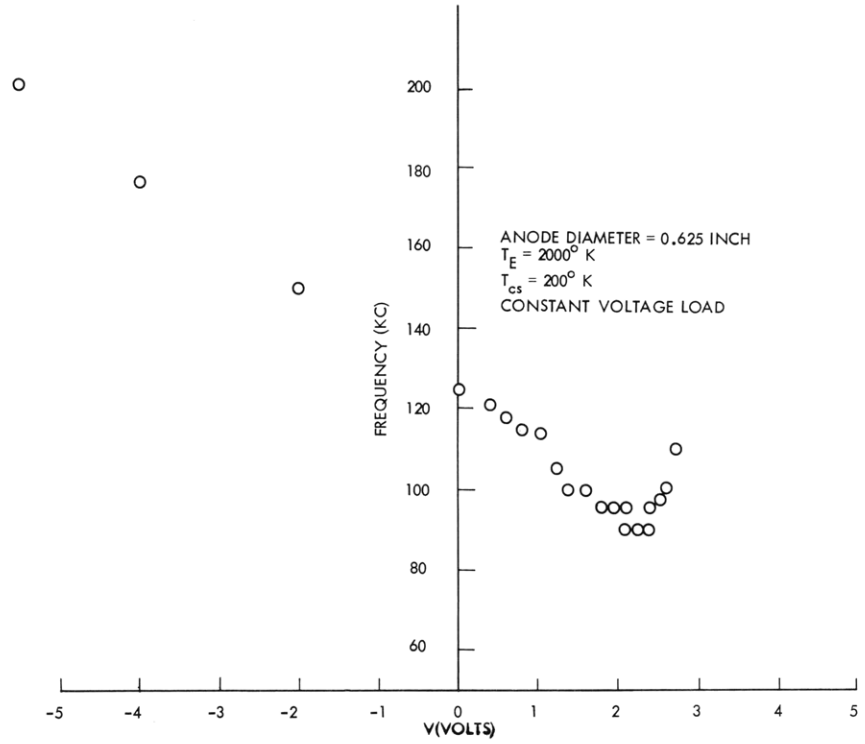

Fig. II-41. Oscillation frequency at various output voltages, constant-voltage load.

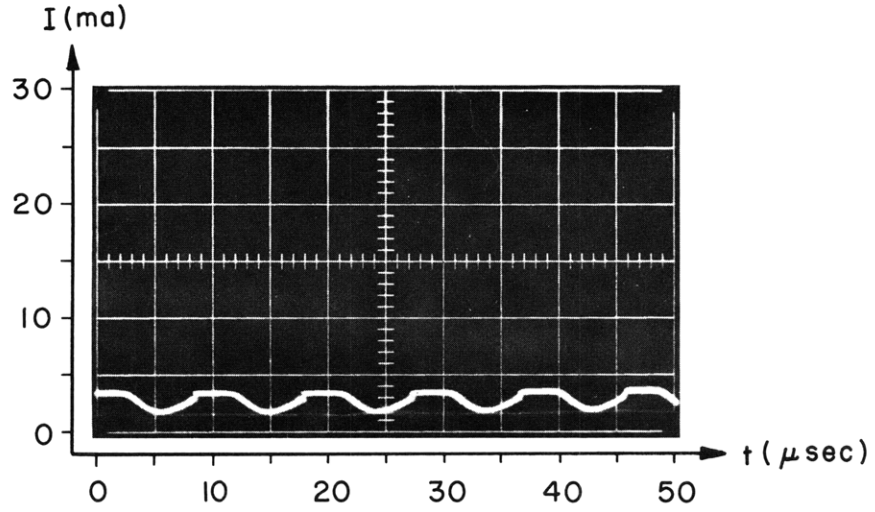

Fig. II-42. Current vs time, constant-voltage load 1.7 volts positive, T_E = 1750°K, T_{cs} = 300°K.

Oscillations under constant-voltage load appeared throughout almost the entire I-V curve as shown in Fig. II-40. These oscillations appeared to be balanced on the I-V curve rather than to be downward surges. The oscillation frequency as a function of the output voltage is shown in Fig. II-41. It is of interest to observe how these oscillations develop. At low emitter temperatures they appear as chopped sine waves, as shown in Fig. II-42. As the emitter temperature increases, they assume a full sine-wave form. The analysis of the mechanism of these oscillations and the analytical expression for the frequency are still being investigated.

M. F. Koskinen

References

1. H. L. Garvin, W. B. Teutsch, and R. W. Pidd, Generation of alternating current in the cesium cell, J. Appl. Phys. 31, 1508 (1960).

2. M. Gottlieb and R. J. Zollweg, Measurements of oscillation frequency and saturation emission currents in cesium diodes, Bull. Am. Phys. Soc. 5, 383 (1960).

3. K. P. Luke and F. E. Jamerson, Oscillations in a filamentary cathode cesium diode converter, J. Appl. Phys. 32, 321 (1961).

3. TEMPERATURE DISTRIBUTION ALONG A STRUT THAT IS LOSING HEAT BY CONDUCTION AND RADIATION

The temperature distribution on, and heat conducted down, a long thin strut that is conducting heat along its length and radiating at the sides was investigated. The problem was greatly simplified by supposing that: (a) the strut is very thin so that the temperature on any cross section is uniform; (b) the properties of the material are supposed to be independent of temperature; and (c) heat exchange between the strut and its surroundings takes place only by heat conduction at the ends and radiation to and from the sides.

The calculations can easily take account of electrical heating of the strut by the passage of current along it; the effect is equivalent, as far as the mathematics is concerned, to raising the temperature of the surroundings. This aspect of the problem has not been dealt with in detail, since the method is clear and we propose to make accurate calculations for various materials, taking into account variations of the gross material properties with temperature, as Langmuir, McLane, and Blodgett[1] did for tungsten filaments.

The equation to be solved is

$$ka\frac{d^2t}{dx^2} = \sigma a\epsilon\left(t^4 - t^4_{\text{surroundings}}\right),$$

where

k, σ, ϵ are the thermal conductivity, Stefan's constant, and the emissivity;

a is the cross-section area;

α is the surface area/unit length;

t is the temperature; and

x is the distance.

The solution is best expressed by using parametric X' and T defined by

$$x = \left\{ \frac{ka}{2\sigma\alpha\epsilon} \frac{T_R^3}{t_{surroundings}^3} \right\}^{1/2} \cdot X'$$

$$t = T \cdot \frac{t_{surroundings}}{T_R}$$

where T_R is a reference temperature for curve plotting, and is equal to the value that T would attain in the middle of an infinitely long bar. For an unheated bar this is equal to room temperature.

The solution of the equation is expressible in the following integral form:

$$\int_{X_1'}^{X_2'} dX' = \int_{T_1}^{T_2} \frac{dT}{\left[\frac{T^5 - T_o^5}{5} - T_R^4 (T - T_o) + Q_o^2 \right]^{1/2}}$$

where $Q_o = \left(\frac{dT}{dX'} \right)_o$ at $T = T_o$.

The equation is of the second order, but the derivative is independent of the absolute value of x. Two boundary conditions need to be specified: two temperatures on the strut and their distances apart, or the temperature gradient and the temperature at a certain point. Thus any particular temperature configuration corresponds to one of a family of curves. The following boundary conditions have been considered for convenient plotting: $T = \infty$ at $x = 0$, and $Q_o = 0$ at $T = T_o$. With these conditions the curves shown in Fig. II-43 have been plotted. The reference temperature T_R for these curves has been chosen equal to 300, and it is always smaller than T.

In order to determine which of the family of curves best represents the distribution under consideration, it is necessary to select that curve which has two conditions corresponding to the given case. The rest of the details of the configuration can be read off the graph, the real values of x and t being derived from the parametric X' and T. Generally, only part of one of the family of characteristics represents the actual temperature distribution along the strut.

A more convenient graph is obtainable and is shown as Fig. II-44. In this chart the

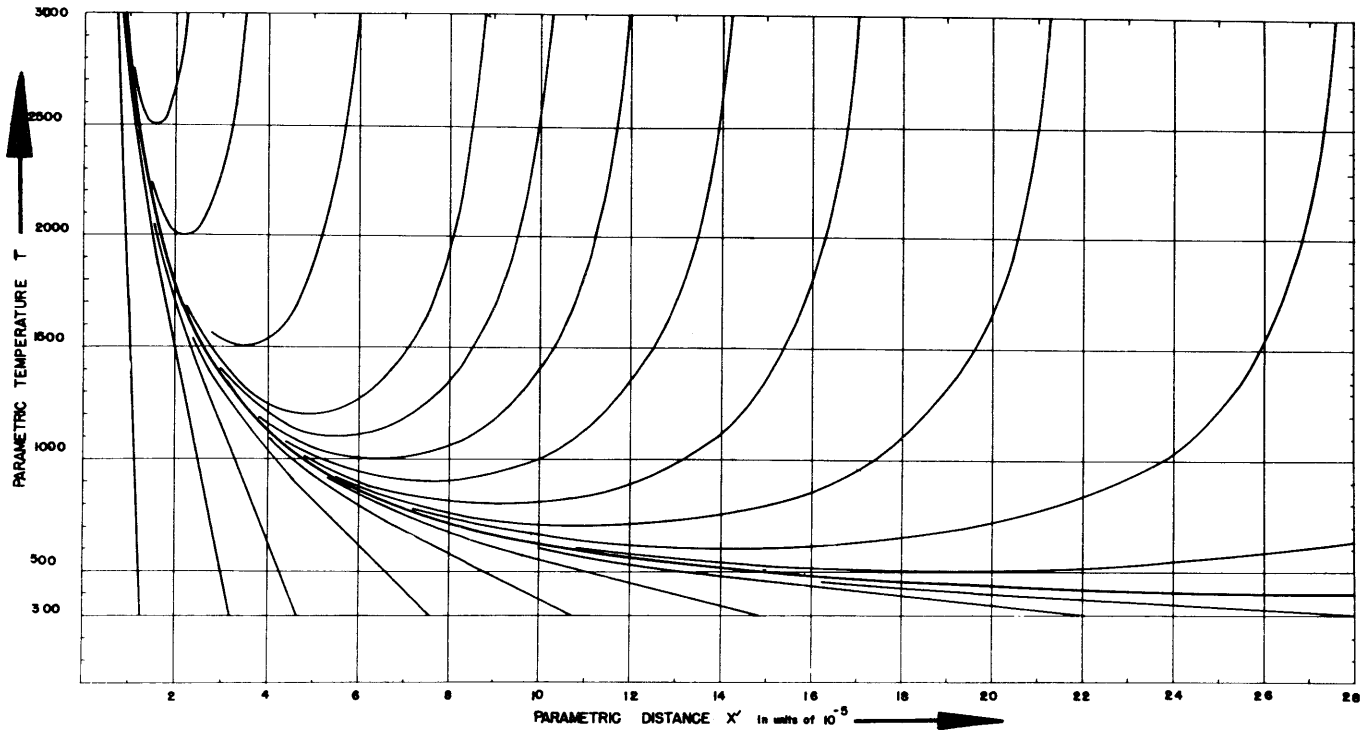

Fig. II-43. Curves of T versus X' for $T > T_R$ and $T_R = 300$.

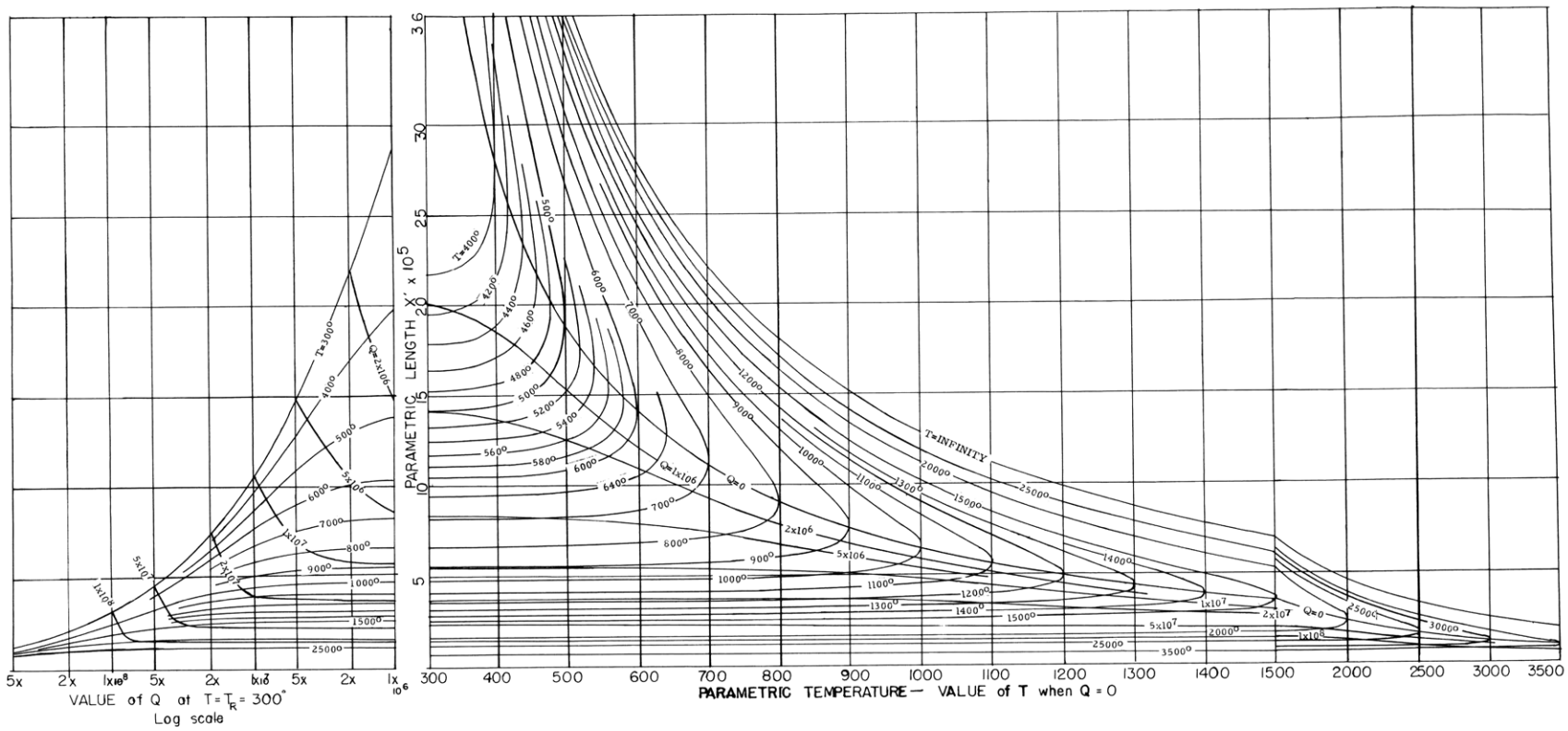

Fig. II-44. Alternative representation of the data of Fig. II-43. On vertical lines different possible temperature configurations were marked off on a bar. The curves join points of equal temperature and equal heat flow. At the bottom of the diagram are marked the leading conditions of the corresponding temperature configuration of the indicated vertical line.

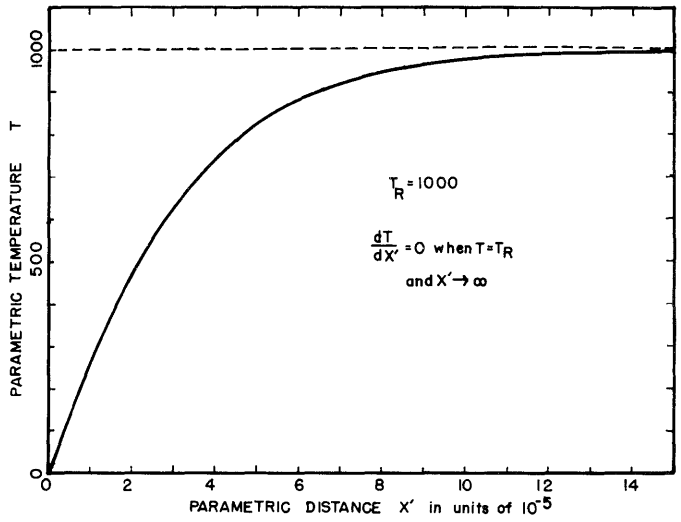

Fig. II-45. T versus X' for the limiting case when $T < T_R$.

temperature distribution for a number of representative configurations were plotted along vertical lines, the lines being arranged so that on the left-hand side of the figure each line corresponds to a certain temperature gradient at room temperature. On the right-hand side are plots for which there is zero temperature gradient at a certain temperature. The special conditions for each line are written against each line across the bottom of the figure. The plots are set in order and evenly so that curves joining points of equal temperature and points of equal temperature gradient may be made. The value of this presentation is that it allows the configuration for a given case to be picked out more simply than would be possible from Fig. II-43, especially since interpolation between the configurations for which calculations have been made is much easier.

It is interesting to note that the temperature approaches infinity for a definite finite value of x; that is, any strut with a zero temperature gradient at a temperature higher than room temperature has a finite length only.

The case of $T < T_R$ is equivalent to the temperature distribution of electrically heated wires with cooled ends. A curve of this sort for which the reference temperature has been chosen as $T_R = 1000$ is shown in Fig. II-45. This is part of the limiting characteristic for which $T = T_R$ when $\frac{dT}{dX'} = 0$.

The M. I. T. Computation Center is thanked for help in the numerical evaluation of the integral.

W. T. Norris

References

1. I. Langmuir, S. McLane, and K. B. Blodgett, The effect of end losses on the characteristics of filaments of tungsten and other materials, Phys. Rev. 35, 478 (1930).

4. MAGNETICALLY DRIVEN T-TYPE SHOCK TUBE OF RECTANGULAR GEOMETRY*

This report is a summary of a Master's thesis[1] submitted by the author to the Department of Mechanical Engineering, M. I. T., June 1961.

With the basic principle of operation of the T-type shock tube in mind, a mathematical model was conceived in order to submit the real phenomena to analysis. This model was based on a sheet distribution of current in a shock tube of rectangular cross section. A theory was developed for the magnetic pressure on the gas in the tube that contains the current sheet and for the resulting shock velocities that would be expected.

A shock tube was designed after the model. Its basic features were: (a) the electrodes that were designed to produce sheet discharges, and (b) the conducting walls lining the two sides of the tube in which the electrodes were inserted. The dimensions of the tube's cross section were 2 cm × 4 cm.

Experiments were performed with hydrogen used as the working gas. Photographs were obtained by using a rotating-mirror camera. An external search coil was used to investigate the location of the current sheet in the tube, and the signal from this coil was correlated with the photographic data. An analysis based on the model was performed on the magnetic field that was expected at the location of the search coil because of the current sheet propagating down the tube, and this theory was compared to the measurement obtained from the coil.

Excellent agreement of theory with experiment was obtained for shock velocities less than 4 cm/μsec, whereas discrepancies as large as 50 per cent between experiment and theory were found for higher shock velocities of approximately 9 cm/μsec.

The nature of the flow of current in the tube was verified.

We conclude that the theory that was developed is useful as a basis for the design of the T-type shock tube. In the thesis to which reference is made, the design of such an instrument is discussed with regard to the desired criterion of operation; that is, one-dimensionality versus higher shock velocity. Also, a novel method of increasing the efficiency of the transfer of electrical energy to the gas is discussed briefly.

L. Y. Cooper

References

1. L. Y. Cooper, On the Magnetically Driven T-type Shock Tube of Rectangular Geometry, S. M. Thesis, Department of Mechanical Engineering, M. I. T., June 1961.

---

*This work was supported in part by the Air Force Cambridge Research Laboratories under Contract AF19(604)-4551.